1

Polymer Spectroscopy – Spectroscopy from the Far-Ultraviolet to Far-Infrared/Terahertz and Raman Spectroscopy

Yukihiro Ozaki[1,2] *and Harumi Sato*[3]

[1] *Kwansei Gakuin University, School of Biological and Environmental Sciences, 2-1 Gakuen, Sanda, Hyogo, 669-1337, Japan*
[2] *Toyota Physical and Chemical Research Institute, Nagakute, Aichi, 480-1192, Japan*
[3] *Kobe University, Graduate School of Human Development and Environment, Higashi-Nada, Kobe, 659-8501, Japan*

1.1 Introduction to Polymer Spectroscopy

Polymer spectroscopy has played a very important role in the investigation of the structure, physical and chemical properties, and reactions of polymers in the last half century [1–9]. As an analytical technique, polymer spectroscopy was born just before World War II and gradually became more commonplace in the 1950s. Throughout the 1950s and 1960s, polymer spectroscopy developed significantly in parallel with the development of infrared (IR) spectroscopy, although Raman spectroscopy was also used in that period [1–4]. The brief history of polymer spectroscopy is described in Preface and this chapter later.

The purpose of this chapter is to provide an overview of polymer spectroscopy. This chapter consists of an outline of polymer spectroscopy, a brief history of polymer spectroscopy, an overview of molecular spectroscopy for polymer research, and a review of examples of studies based on polymer spectroscopy. In the last part of this chapter, we describe the perspectives for polymer spectroscopy.

1.1.1 Outline of Polymer Spectroscopy

Polymer spectroscopy is largely based on optical spectroscopy, which involves spectroscopy in the ultraviolet (UV), visible (Vis), and IR regions. The UV region ranges from 10 to 380 nm and may be divided into four regions: vacuum ultraviolet (VUV, 10–120 nm), far-ultraviolet (FUV, 120–200 nm), deep ultraviolet (DUV, 200–300 nm), and UV (300–380 nm) [10]. Spectroscopy in the UV region is important because it provides the electronic spectra of molecules. However, compared with IR spectroscopy, UV spectroscopy has rarely been used for polymer research. Further, recently, among the UV regions, FUV spectroscopy has been applied to polymers to investigate the electronic and molecular structure and intermolecular

Spectroscopic Techniques for Polymer Characterization: Methods, Instrumentation, Applications,
First Edition. Edited by Yukihiro Ozaki and Harumi Sato.

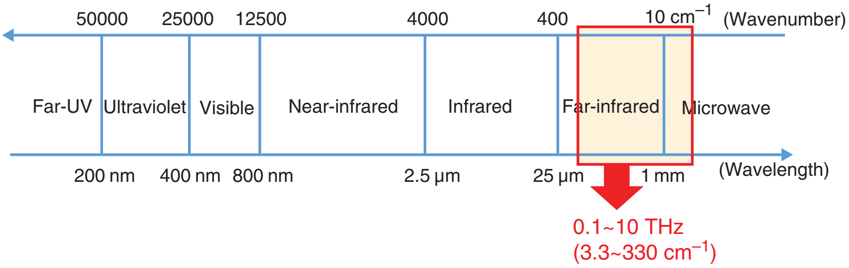

Figure 1.1 The region of electromagnetic wave from 200 nm to 1 mm.

interactions of polymers [11–14]. In Chapter 6, FUV studies of polymers are introduced. In addition, UV resonance Raman spectroscopy has also been used to investigate polymer structure and functions and will be reviewed in Chapter 7.

The IR region (800 nm to 1 mm, 12 500 to 10 cm^{-1}) is so wide in terms of energy that it is divided into three regions: near-infrared (NIR, 800–2500 nm) [15–17], IR (or mid-infrared; MIR, 4000 to 400 cm^{-1}) [18–20], and far-infrared (FIR, 400 to 10 cm^{-1}) [21, 22], as shown in Figure 1.1. Spectroscopic techniques in these regions have developed independently over the years, although the developments of NIR and FIR spectroscopies generally remained far behind those of IR (MIR) spectroscopy. However, in the last three decades, remarkable developments have been made in NIR spectroscopy [15–17]. Recently, advances in FIR spectroscopy have also been made. For example, terahertz spectroscopy was initiated at the end of the 1990s because of developments in new light sources and detectors in the FIR region [23–25].

IR, NIR, and FIR/terahertz spectroscopies are basically vibrational spectroscopic techniques [26]. IR spectroscopy is concerned mainly with fundamental vibrational modes [18–20], NIR spectroscopy is the spectroscopy of overtones and combinations of fundamentals [15–17], and FIR/terahertz spectroscopy treats low-frequency vibrational modes such as skeletal vibrations, torsional vibrations, and lattice vibrations [23–25]. Crucially, IR spectroscopy also involves the overtones and their combinations, NIR spectroscopy is concerned with electronic spectroscopy, and FIR/terahertz spectroscopy involves rotational spectroscopy. Thus, there is a clear border between IR and NIR spectroscopy because NIR spectroscopy is not related to the fundamentals; in contrast, the border between IR and FIR is not always clear. However, IR, NIR, and FIR spectroscopies are not three sisters; rather, IR is the mother of NIR spectroscopy because the overtones and combinations originate from the fundamentals.

Visible spectroscopy is typically only used as an ancillary tool in polymer studies, for example, to study the electronic structure of conductive polymers (Chapter 13). As an optical spectroscopic technique, fluorescence spectroscopy is also used for polymer research but is not considered in this book. In addition to the above optical spectroscopies, Raman spectroscopy is very important in polymer studies [27–30]. This is one of the key spectroscopic techniques in polymer research. In this book, normal Raman spectroscopy, resonance Raman spectroscopy, UV-resonance Raman spectroscopy, surface-enhanced Raman scattering (SERS) [31–33], tip-enhanced Raman scattering (TERS) [31–33], and Raman imaging [34] are introduced as important tools for polymer science. In addition, there is no doubt that nuclear magnetic resonance (NMR) spectroscopy is very important in polymer spectroscopy, but it is beyond the scope of this account.

1.1.2 Brief History of Polymer Spectroscopy

In the second part of this chapter, we provide an overview of the history of polymer spectroscopy in relation to the 100th anniversary of polymer theory in 2020. Just before World War II, studies of polymers vibrational spectroscopy started [18–20]. For example, Kirkwood [35] and Whitcomb et al. [36] performed normal vibrational calculations on polyethylene. After World War II, developments in IR spectroscopy progressed significantly because of advances in its light sources, spectrometers, and detectors. Therefore, even in the 1940s, many polymer scientists started using IR spectroscopy for polymer studies. For example, Shimanouchi et al. [37] reported normal vibrational calculations of polyethylene. Many pioneering papers on IR studies of polymers were published in the 1950s. Shimanouchi [38], Krimm [39], Eliot [40], and Hummel [41] conducted systematic studies on the vibrational spectra of polymers. Of course, there were many other scientists who advanced polymer spectroscopy in the 1950s. In particular, several important books concerning the IR spectra of polymers were published in this period [5]. Eliot [40] wrote a very important review of polymer spectroscopy in 1960, and, in the 1960s, many research groups were involved in IR studies on the characterization of polymers [4].

In the 1960s, Schachtschneider and Snyder [42] conducted normal vibrational calculations on polyethylene; Tasumi and Shimanouchi[43] studied the vibrational spectroscopy of polyethylene using the modified Urey–Bradley force field; and Miyazawa and coworkers [44] reported IR studies of polyoxymethylene, polyethylene glycol, polypropylene, and polyethylene and also introduced neutron scattering in these studies [45]. Tadokoro and coworkers [46] investigated the IR spectra of polyoxycyclobutane, polyamides, and other polymers in the 1960s. They also published several papers on FIR studies of polymers, such as polyamides and polyesters [47]. Krimm and Bank [48] also reported FIR studies on polyethylene.

In contrast, Raman spectroscopy studies of polymers started with those of long-chain *n*-alkanes. For example, Mizushima and Shimanouchi [49] reported the Raman spectrum of *n*-paraffin in 1949, and Hendra [50], Koenig [51], and others were involved in Raman studies of polymers in the 1960s. Since the introduction of lasers to Raman spectroscopy at the end of the 1960s, Raman studies of polymers have shown enormous progress [4, 5]. For example, the longitudinal modes (LAM) of polymers were investigated using Raman spectroscopy by Mizushima and Shimanouchi [49] and later by Schaufele and Shimanouchi [52] for a series of *n*-alkanes. Studies on LAM have been conducted in several directions, including the investigation of the effects of interactions at the lamella interface on the LAM frequencies. Stroble and Eckel [53] and Hsu and Krimm [54] made prominent contributions to these studies.

In the latter half of the 1950s and 1960s, several interesting NIR studies of polymers were reported [4]. For example, in 1956, Miller and Willis [55] used an NIR method for the analysis of butadiene–styrene copolymers based on the evaluation of the aromatic and aliphatic CH combination bands at 4580 and 4250 cm^{-1}, respectively. Takeuchi et al. [56a] used NIR spectroscopy to predict the acrylonitrile content in styrene–acrylonitrile copolymers. Tosi [56b] found a correlation between the frequency of the first overtone of the CH_2 stretching mode at 5800 cm^{-1} and the copolymer composition and interpreted the results in terms of the methylene sequence lengths of the ethylene–propene copolymers prepared using different catalysts. Many researchers have employed NIR spectroscopy for the investigation of polymeric structures and analytical purposes [4].

In this report, we do not describe the history of vibrational spectroscopy of polymers since the 1970s because many research groups have published excellent studies. However, it is important to mention two renaissances of vibrational spectroscopy that occurred in and after the 1970s. One is the introduction of lasers to Raman spectroscopy [28–30]. This made Raman experiments much easier and enabled various kinds of Raman spectroscopy, such as resonance Raman spectroscopy, SERS, Raman microscopy, and time-resolved Raman spectroscopy. Another is the development of Fourier transform (FT)IR in the 1970s and 1980s [18, 19]. This made IR measurements much easier and more precise. Moreover, various kinds of IR spectroscopy were born because of the development of FTIR spectroscopy; for example, micro-IR, time-resolved IR, and photoacoustic IR. These two renascences were truly great events that opened the doors for current vibrational spectroscopy.

1.2 Overview of Molecular Spectroscopy from the Far-Ultraviolet to Far-Infrared/Terahertz and Raman Spectroscopy in Polymer Research

In this chapter, because the characteristics and applications of IR and Raman spectroscopy in polymer research are reported in many chapters of this book and have been discussed in many other studies, we only provide a brief overview [4–9]. We describe the characteristics and applications of FIR/terahertz/low-frequency Raman spectroscopy, NIR, FUV, SERS, and TERS in polymer studies. Although applications of FIR/terahertz/low-frequency Raman spectroscopy, NIR, and FUV are introduced in Chapters 4–6, respectively, a description of them is presented in this chapter.

1.2.1 IR and Raman Spectroscopy Analyses

IR [18–20] and Raman spectroscopy [28–30] are key vibrational spectroscopies. They are mainly concerned with fundamental vibrational modes, although some bands arising from overtones and combinations of fundamentals also appear in both spectra. IR and Raman spectroscopy are often complementary, and the differences between IR and Raman spectroscopy lie in their selection rules. One of the two selection rules in IR spectroscopy is that a vibrational mode that experiences a change in the dipole moment during a molecular vibration is IR active, whereas that of Raman spectroscopy is that a vibrational mode with a change in molecular polarizability during a vibrational mode is Raman active. In general, asymmetric vibrations yield strong IR absorptions, whereas symmetric vibrations give rise to intense Raman bands. In IR spectra, bands arising from the stretching modes of polar functional groups such as $C=O$, OH, and $C=N$ and bands arising from local vibrations, such as the CH_2 scissoring mode, are intense, whereas bands derived from a whole molecule or a large part of the molecule are weak. In Raman spectra, bands arising from the stretching modes of heavy atoms, such as S–S, C–S, and C–Cl stretching, are strong. In addition, bands originating from the stretching modes of multiple bonds, such as those arising from $C=C$, $N=N$, and $C\equiv N$ stretching modes, are strong, and in-phase vibrations derived from a whole molecule or a large part of the molecule produce intense bands in Raman spectra. The ring-breathing mode of the benzene ring and the accordion vibrations of long-chain molecules are good examples of these.

IR spectroscopy uses IR absorption, as well as IR reflection (e.g. attenuated total reflectance [ATR], external reflection, reflection–absorption [RA], diffuse reflectance [DR], emission, and photoacoustic spectroscopy) [18–20]. Among them, ATR and RA spectroscopies are particularly useful for polymer research. An IR spectrometer can also be connected to optical microscopy (micro-IR, Chapter 2) and atomic force microscopy-infrared (AFM-IR) equipment, as well as other instruments. The polarized IR spectra of stretched polymers are useful for investigating the molecular and crystal structures of polymers, particularly their orientation [4, 5, 7, 8]. IR spectroscopy is also useful for studying the crystallinity, and so-called crystallization-sensitive bands can be used as indicators of crystallinity [4, 5, 7, 8]. The symmetry properties of polymers can be used to analyze their vibrational spectra.

Raman spectroscopy is a nondestructive analytical tool that enables the in situ analysis of a sample in its original form, and it is possible to use fiber optics for the Raman measurements. There are various kinds of Raman spectroscopy [28–30]; among them, normal Raman, Raman microscopy, Raman imaging, SERS, and TERS are often used for polymer studies. Resonance Raman spectroscopy has been used to study conductive polymers (Chapter 13). UV resonance Raman spectroscopy has recently been employed to study polymers (Chapter 7), and polarized Raman spectroscopy is useful for molecular orientation studies. In this chapter, we will demonstrate examples of normal Raman spectroscopy, Raman imaging, and TERS.

In polymer research, IR and Raman spectroscopies yield information about the chemical nature and physical properties [4–8]. Concerning the chemical nature, each spectroscopic method is useful, for example, for the identification of polymers and the investigation of structural units and the type and degree of branching. It is also possible to identify additives and impurities. As for the latter, both spectroscopic techniques give rise to information about stereoregularity, conformational order, polymer orientation, hydrogen bonding, intermolecular interactions, lamellar thickness, and state of order such as crystalline and amorphous (AMP) phases. Polymer reactions can also be monitored using both IR and Raman spectroscopies.

1.2.2 FIR/Terahertz and Low-Frequency Raman Spectroscopy

The low-frequency region is of great interest in the studies of the state of order of polymers because low-frequency modes often reflect the structure of the backbone and the intermolecular interactions of the polymers [4, 5]. In the low-frequency region, the following types of vibrations are observed.

1. Stretching vibrations of heavy atoms, e.g. I–I stretching mode.
2. Bending vibrations of the polymer skeletons.
3. LAM.
4. Torsional vibrations.
5. Lattice vibrations (intermolecular vibrations between adjacent chains within a crystallographic unit cell).

In recent years, low-frequency vibrational spectroscopy has become a subject of keen interest because of the marked progress in terahertz time-domain spectroscopy (THz–TDS) [23–25] and low-frequency Raman spectroscopy using volume Bragg notch filters. Currently, high-quality low-frequency spectra (FIR, THz–TDS, Raman) of various materials can be obtained, allowing the investigation of high-order conformations, crystal polymorphism, intermolecular interactions including hydrogen bonds, and the dynamics of various systems. As targets of these techniques, polymers are particularly interesting because their low-frequency vibrational modes can sharply reflect the interchain interactions and higher-order polymer conformations [57] (Chapter 4). In this chapter, we will introduce an FIR, low-frequency Raman, and quantum chemical calculations of nylon-6 in detail [57d]. Moreover, Chapter 4 reports the low-frequency vibrational spectroscopy of polymers.

1.2.3 Near-Infrared (NIR) Spectroscopy

The applications of NIR spectroscopy to polymer studies began with quantitative analysis of polymers, such as the determination of the hydroxyl number, water content, and residual carbon–carbon double bonds [4]. Since chemometrics and optical light fibers were introduced to the analysis of the NIR region, the usefulness of NIR spectroscopy in polymer research and analysis has dramatically increased (Chapter 5 and this chapter). Currently, NIR spectroscopy is widely used as a nondestructive and in situ analytical and structural probe of polymers [4, 15, 16]. One of the most active applications of NIR spectroscopy to polymers is online analysis and quality control using NIR light-fiber optic spectroscopy [58, 59], although there are many other applications, some of which are described in Chapter 5.

Although the practical applications of NIR spectroscopy in the polymer industry are extensive, an understanding of the principles behind their analysis remains insufficient. Recently, efforts to unravel complicated NIR spectra more clearly and to interpret the chemometrics models involved have taken several directions [15]. One is the systematic study of the NIR spectra of various polymers from the perspective of basic studies such as those of hydrogen bonding [60]. Another direction is the theoretical study of the assignment of bands arising from overtones and combinations in the NIR spectra of molecules using density functional theory (DFT) calculations [61].

1.2.4 SERS and TERS Spectroscopy

SERS is sensitive to single molecules and is molecule-specific and, thus, has been used in materials science, biomedical science, surface science, environmental analysis, and beyond [31–33]. The enormous enhancement of SERS signals arises mainly from two mechanisms: electromagnetic (EM) and charge-transfer (CT) effects. EM enhancement stems from localized surface plasmon resonance on a metal substrate, whereas CT enhancement is a resonance-like process in which the CT resonance depends on the energy difference between the Fermi level of a metal substrate and the molecular orbitals of an adsorbate.

Recent rapid progress in TERS has resulted from developments in nanotechnology [33], which has enabled spectral measurements with a spatial resolution below 10 nm and control at the single-molecule level. Currently, in nanotechnology, measurements are frequently based on scanning tunneling microscopy (STM), scanning electron microscopy (SEM), and transmission electron microscopy (TEM), but these methods cannot provide information about molecular structure. On the other hand, TERS has very high spatial resolution and, at the same time, allows one to explore molecular structure. TERS is the product of the organic integration of scanning probe microscopy (SPM) techniques and a plasmon-enhanced effect.

SERS suffers from a limited spatial resolution of hundreds of nanometers owing to the diffraction of light. Therefore, the information obtained from SERS is the average of large amounts of different surface sites. On the other hand, TERS is a newly developed Raman technique with spatial resolution beyond the diffraction limit of light; it can provide site-specific information and can be performed on any material surface regardless of morphology. TERS can be applied in various environments, such as ambient air, ultrahigh vacuum, solutions and liquids, and electrochemical environments. An example of a TERS study is reviewed in this chapter.

1.2.5 FUV Spectroscopy

FUV spectroscopy is concerned with electronic transitions, as in the case of DUV and UV spectroscopy, but FUV spectroscopy is clearly different from the other UV spectroscopies [10–12]. First, in contrast to the DUV and UV regions, which are free from oxygen absorption, the FUV region requires either a vacuum evaporation system or a nitrogen-gas-purging system. In the DUV and UV regions, absorption bands originating from various types of lower-energy electronic transitions, such as π–π^* and n–π^* transitions, can be observed, but higher-energy n–σ^* transitions and Rydberg transitions do not appear, whereas in the FUV region, in addition to the bands arising from π–π^* transitions, those from n–σ^* and σ-Rydberg transitions are observed [10–12]. Compared with that of DUV spectroscopy, the development of FUV spectroscopy of the condensed phase has made very slow progress. The main reason for this is the very high absorptivity of molecules in the FUV region [10–12]. To overcome this difficulty, we introduced the ATR technique to the FUV region [10–12]. The ATR technique allows the measurement of spectra similar to those of transmittance spectra with a very short optical path length. The development of ATR–FUV spectrometers has enabled the measurement of the spectra of liquid and solid samples in the nearly full FUV region without problems such as peak saturation. ATR–FUV spectroscopy has been recently applied to polymer studies to investigate the structure, electronic transitions, hydrogen bonds, and intermolecular interactions of polymers [13, 14]. Chapter 6 reports some examples of FUV studies on polymers.

1.3 Specific Examples of Molecular Spectroscopy Studies of Polymers

In this chapter, six examples of molecular spectroscopic studies of polymers are reviewed. They include the applications of IR, Raman, NIR, FIR, low-frequency Raman, TERS, Raman, and SERS imaging studies.

1.3.1 Infrared, Raman, and NIR Spectroscopic Evidence for the Coexistence of Hydrogen Bond Types in Poly(Acrylic Acid)

Dong et al. [62] used IR, Raman, and NIR spectroscopies to reveal the coexistence of various types of hydrogen bonds in poly(acrylic acid) (PAA) (Figure 1.2). The IR, Raman, and NIR spectra of a cast film of PAA were measured between 40 and 140 °C to investigate the hydrogen bond structures and their dissociation. The different hydrogen bond structures persisted even when the temperature rose well above the glass transition temperature. The Raman spectra confirmed the presence of different types of hydrogen bonds. It was found from the temperature-dependent intensity changes in the band arising from the first overtone of the OH stretching mode of PAA that the COOH groups dissociate significantly at high temperatures. Dong et al. [62] revealed the coexistence of various possible hydrogen bond forms analogous to those in the small aliphatic acids in PAA (Figure 1.2). The oligomeric chains of the COOH groups in PAA may explain the previously proposed cooperative hydrogen bonds in PAA or polymer blends containing PAA.

PAA and its copolymers are very useful as thickening agents for latexes and adhesives, as well as ingredients in pharmaceutical, cosmetic, coating, and agricultural chemical formulations. As part of the investigation of the interesting properties of PAA, for example, its special viscosity behavior in solutions, many researchers have extensively studied the conformational changes and hydrogen bonds between the macromolecular chains [63, 64]. The hydrogen bonds in PAA play a major role in determining its properties. Using IR, Raman, and NIR spectroscopy, it was found that although PAA is usually assumed to be strongly self-associated, it is a complex hydrogen-bonded mixture with a considerable number of dissociated species [62].

Figure 1.3 shows the temperature-dependent IR spectra of PAA in a cast film measured from 40 to 140 °C [63, 64]. As shown in Figure 1.3, the IR spectrum of PAA is characterized by a broad OH stretching band (3600 to 3000 cm^{-1}), overtones and combinations of bands at 1413 and 1248 cm^{-1} enhanced by Fermi resonance with the broad OH stretching band, $C = O$ stretching bands (1750 to 1700 cm^{-1}), and relatively broad and conformationally sensitive backbone bands (1500 to 800 cm^{-1}) [62]. Based on the comparison of the spectra in Figure 1.3 with previously reported

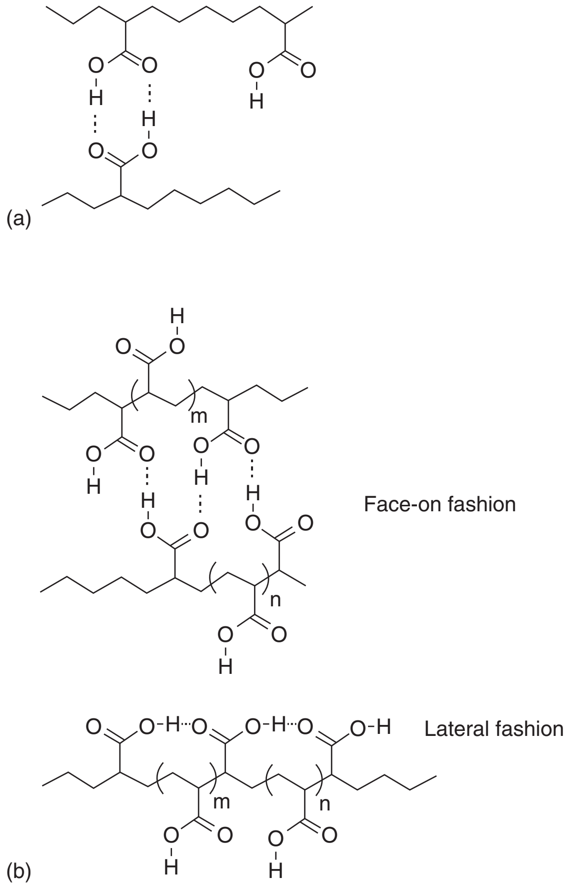

Figure 1.2 Four possible hydrogen-bonding arrangements of the carboxylic acid groups of PAA. (a) Cyclic dimer and free monomer of COOH groups. (b) Inner and terminal COOH in linear oligomeric forms. Source: Dong et al. [62].

IR spectra of PAA, it was found that the spectra in Figure 1.3 are a result of nearly atactic PAA.

Figure 1.4a,b shows an enlargement of the C = O stretching band region measured at 40 and 140 °C, respectively [62]. Figure 1.4c,d displays the second derivatives of the spectra in Figure 1.4a,b, showing three bands for both spectra collected at 40 and 140 °C. Dong et al. [62] determined the number of band components contributing to the band envelope in the 1800 to 1600 cm^{-1} region to be four using principal component analysis (PCA) [62].

Figure 1.4a,b also shows the results of curve fitting. These results suggest the presence of four bands in this region. For all the spectra obtained from 40 to 140 °C, four bands gave the best fit for the CO envelope, whereas a three-band fit always left some discrepancy. The resolved spectra shown in Figure 1.4a,b yielded four component bands at 1686, 1705, 1723, and 1742 cm^{-1} for the sample at 40 °C and those at 1699, 1706, 1725, and 1743 cm^{-1} for the sample at 140 °C, respectively. The bands at 1705 and 1742 cm^{-1} were assigned to the C = O stretching modes of the cyclic hydrogen-bonded COOH group in the dimeric form and free (non-hydrogen-bonded) COOH group, respectively (Figure 1.2a) [62]. The position

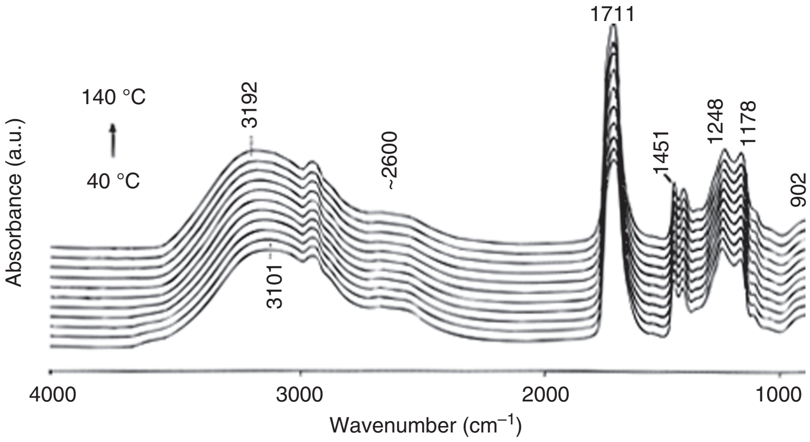

Figure 1.3 FT-IR spectra of PAA measured from 40 to 140 °C (10 °C intervals at rate of 1 °C min^{-1}). Source: Dong et al. [62].

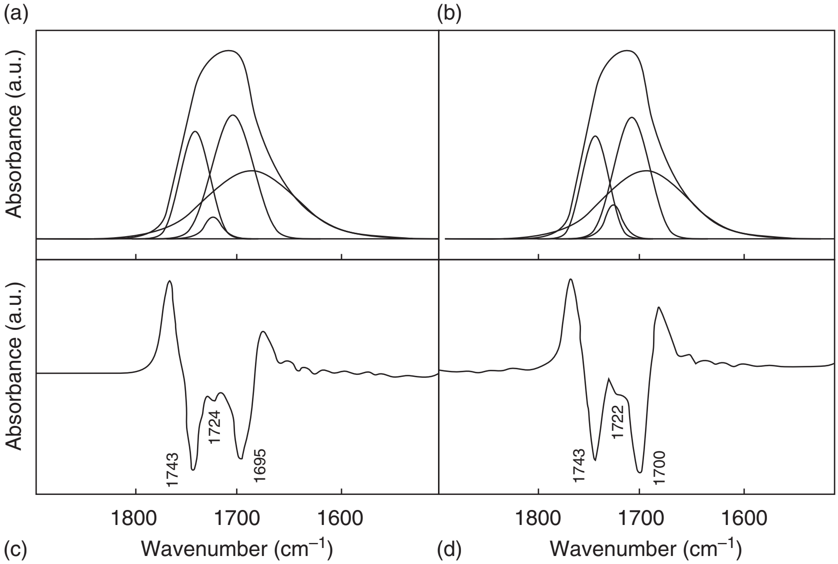

Figure 1.4 FT-IR spectra of PAA in the C = O stretching region measured at (a) 40 and (b) 140 °C; (c) second derivative of spectrum (a); and (d) second derivative of spectrum (b). Curve-fitting results are also shown in the spectra (a) and (b). Source: Dong et al. [62].

of the free C = O band near 1742 cm^{-1} changes little with temperature and is very close to those previously found for free COOH groups in various systems. The frequency of the C = O asymmetric stretching band of the cyclic dimer changes little with temperature because of its fixed configuration.

Of interest is the appearance of a C = O band near 1685 cm^{-1}. This band shifts to the higher-energy side with increase in temperature. The band at 1685 cm^{-1} suggests the presence of an additional hydrogen bond. Several research groups have investigated the structure of self-associated acetic acid using various techniques

[65, 66]. Based on their studies, the C = O band near 1686 cm^{-1} can be ascribed to the inner hydrogen-bonded groups of the oligomeric COOH groups, whereas the residual band near 1725 cm^{-1} was assigned to the terminal group in the oligomeric COOH chains (Figure 1.2b). Of note is that the C = O band widths of the inner hydrogen-bonded groups are much broader than those of other species, reflecting a broad distribution of oligomer chains with variable lengths. Moreover, Dong et al. [62] considered that the less restricted motion of the linear dimeric/oligomeric COOH compared to that of the cyclic dimer results in a slightly lower frequency observed for linear dimer/oligomers. In addition, it is very likely that the C = O groups in the oligomeric chains couple with two adjacent C = O groups in contrast to the C = O group in the cyclic dimer, in which only two C = O groups couple with each other. This may also account for the appearance of the C = O stretching band of the oligomers on the lower wavenumber side than that of the cyclic dimer species [62].

Tanaka et al. [66] compared the dissociation of PAA with that of its monomer analogs in aqueous solutions and found that the dissociation of COOH groups into free species is less favorable for PAA than that for glutaric acid (model compound for the dimer of the PAA repeating unit) and 1,3,5-pentanetricarboxylic acid (model compound for the trimer of the PAA repeating unit). They suggested that some sort of cooperative or nonadditive hydrogen bond is formed in PAA solutions, which makes the dissociation more unfavorable than that in its monomer analogs. Dong et al. [62] proposed that the oligomerization of COOH groups in two- or three-dimensional arrays of the group linkage may account for such cooperative hydrogen bonds.

The Raman spectrum of PAA is shown in Figure 1.5 [62]. In the enlarged Raman spectrum shown in Figure 1.6a [62], an asymmetric broad band arising from C = O stretching modes was observed around 1690 cm^{-1}. The second derivative of the spectrum in Figure 1.6b shows at least three bands in the C = O stretching region, whereas the curve fitting gives four bands at 1742, 1715, 1680, and 1660 cm^{-1}. The

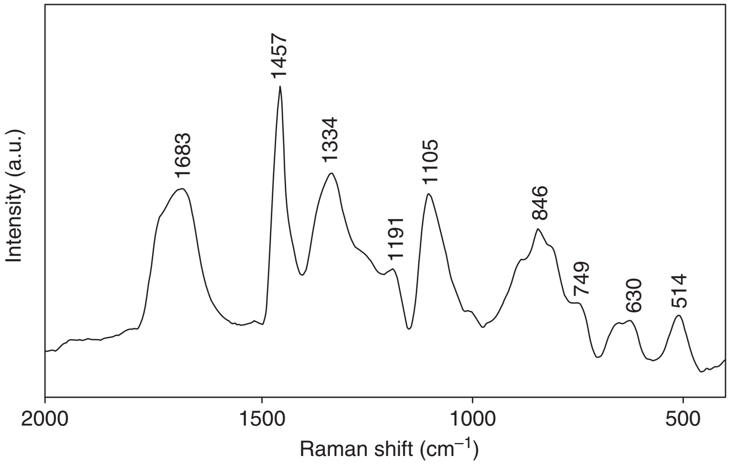

Figure 1.5 An FT-Raman spectrum of PAA measured at 64 °C. Source: Dong et al. [62].

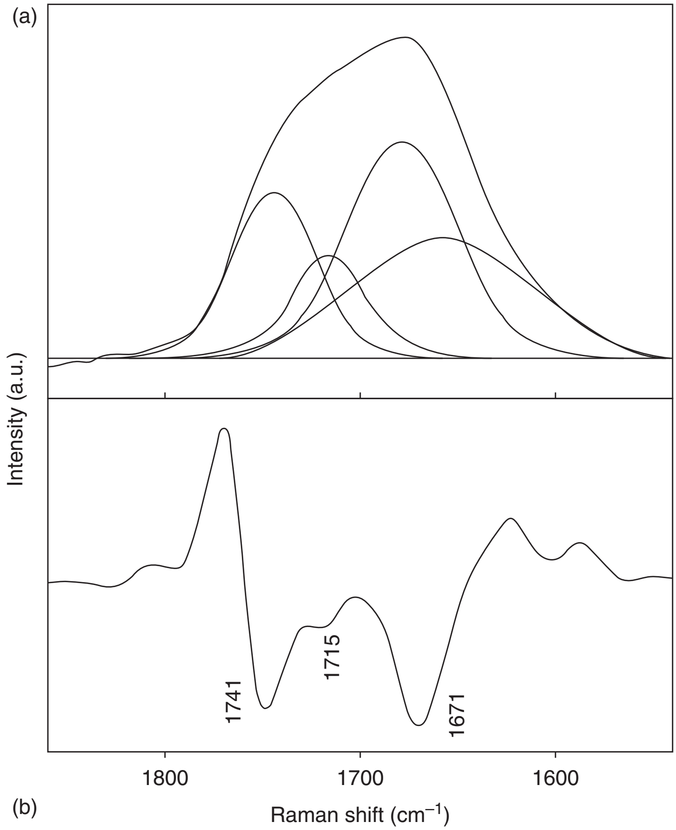

Figure 1.6 Enlarged Raman spectrum of PAA between 1850 and 1550 cm^{-1} showing the components contributing to the C = O stretching band: (a) a curve-fitting result and (b) second derivative plot. Source: Dong et al. [62].

1680 cm^{-1} band was assigned to an in-phase C = O stretching vibration of the cyclic dimer form, whereas the other bands at 1742, 1715, and 1660 cm^{-1} were ascribed to the C = O stretching modes of free COOH and terminal and inner hydrogen-bonded COOH in the oligomeric forms, respectively [65, 66]. It should be noted that the frequency of the dimer species in the Raman spectrum does not coincide with the counterpart in the IR spectrum. However, this observation is reasonable because the Raman band originates from a normal mode involving in-phase $(CO)_2$ stretching, whereas the IR band results from the out-of-phase $(CO)_2$ stretching in the dimer.

Coleman et al. [67] investigated various kinds of hydrogen-bonding species in polymers and adopted Flory's lattice filling methodology to describe two sets of chains, one covalent and the other hydrogen bonded, both of which share the same segments. Interestingly, the association of the repeating units is independent of the covalent chain length and can be treated as a “small” molecule (one containing a single functional group) of equal molar volume. Dong et al. [62] postulated that the hydrogen bond structure in the oligomeric forms takes a face-on arrangement [65, 66] for acetic acid, propionic acid, and *n*-butyric acid or a lateral arrangement [68, 69] for fatty acids adsorbed on a solid surface (Figure 1.2b). It is rather difficult to distinguish these two types of arrangements by IR and Raman measurements, and, thus, it was difficult to conclude which arrangement of COOH chains is favored in PAA. It should be noted that the formation of oligomeric COOH groups does not require hydrogen bonding between the adjacent repeating units in the same hydrocarbon chain because both oligomers and dimers can be formed between COOH groups located on different parts of the chains, as shown in Figure 1.2b.

The species formed by monomeric COOH groups are not well resolved in the IR OH stretching and C = O stretching regions in IR and Raman spectra. Thus, NIR spectroscopy has been used to clarify these species. Figure 1.7 shows the FT–NIR transmission spectra of PAA measured over a temperature range of 40–140 °C [62]. The broad band at around 6820 cm^{-1} is due to the first overtone of the OH stretching mode of the free carboxylic group. The long tail on the lower wavenumber side of this band can be attributed to the terminal free carboxylic groups in the oligomeric forms with different chain lengths. The intensity of the tail increases with temperature, which can be easily verified from the difference spectra of this region. In the NIR region, bands due to hydrogen-bonded OH groups are extremely weak, whereas those arising from the free OH group are relatively strong. The large displacement of the relatively light proton in the free OH group allows it to be in the "free" state relative to the hydrogen-bonded OH groups, resulting in a greater breakdown of the harmonic oscillator approximation and, hence, the selection rules that, in principle, do not permit the appearance of overtones and combinations of bonded species.

As can be seen from the enlargement of the 7000 to 6300 cm^{-1} region (the inset in Figure 1.7), the intensity of the 6820 cm^{-1} band gradually increases with temperature. Broad bands in the 4600 to 4500 and 4060 to 4030 cm^{-1} regions, both associated with COOH combination vibrations, also increase with temperature, whereas the intensities of other bands irrelevant to the COOH group vibrations are temperature independent [62]. In the inset of Figure 1.7, the band area of the free COOH species increases significantly above 100 °C. It is quite reasonable that above the glass transition temperature (T_g) of PAA, the segmental motion accelerates the considerable gain of the free COOH groups as the macromolecular chains disentangle at the expense of the hydrogen-bonded forms. In the IR region, neither the OH stretching band arising from free COOH (near 3500 cm^{-1}) nor the intensity change of the free COOH group (the 1742 cm^{-1} band) is clearly detectable. However, this is not a problem in the NIR region.

In this study, IR, Raman, and NIR spectroscopy were utilized to explore the hydrogen bonding in PAA [62]. In addition to the presence of monomer and cyclic dimer forms of COOH, additional spectral features were interpreted in terms of the presence of oligomeric species. The coexistence of various hydrogen-bonded species of the COOH groups in PAA may provide new insights into the thickening mechanism of the polymer.

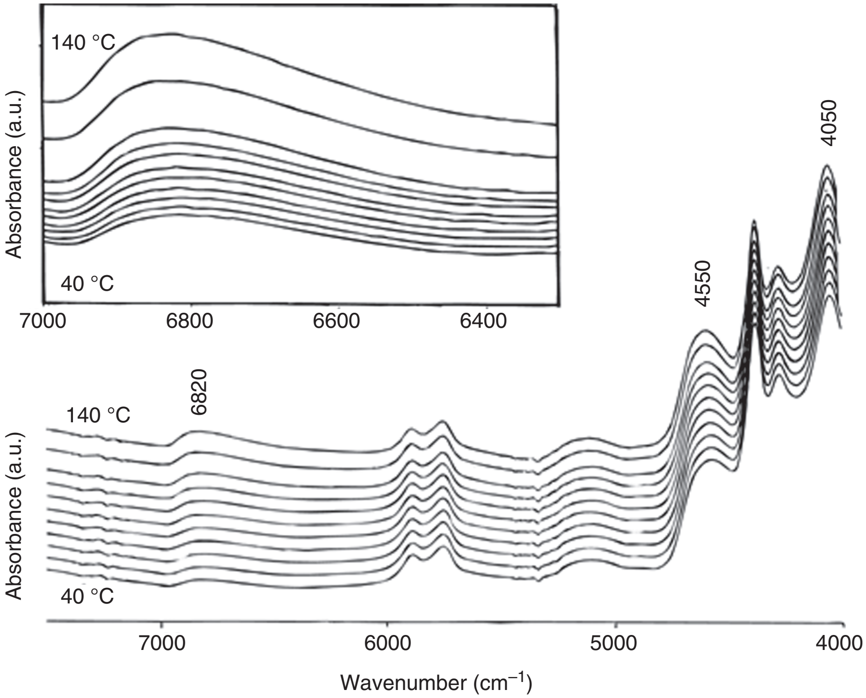

Figure 1.7 FT-NIR spectra of PAA measured from 40 to 140 °C (in 10 °C intervals at a rate of 1 °C min^{-1}). Inset: enlarged NIR spectra showing the first overtone of an OH stretching mode. Source: Dong et al. [62].

1.3.2 Low-Frequency Vibrational Modes of Nylon-6 Studied by Using IR and Raman Spectroscopies and Density Functional Theory Calculations

Low-frequency vibrational spectroscopy has recently been used extensively to investigate the structures and physical properties of polymers [57d]. In Chapter 4, one can find several good examples of this subject; here, we present one example. Figure 1.8 shows the FIR spectra in the region of 350 to 50 cm^{-1} of (a) nylon-6 in the α-form measured in the temperature range of 29–194 °C and (b) their second derivative spectra at 29 and 194 °C [57]. The FIR spectrum of nylon-6 at 29 °C shows characteristic crystalline bands at 294, 222, and 111 cm^{-1} (Figure 1.8a). In the region of 125 to 80 cm^{-1}, as the temperature increased, the maximum peak position shifted to 98 from 111 cm^{-1} with a decrease in intensity at 111 cm^{-1}. The second-derivative spectra indicate that the position of the band at 111 cm^{-1} changes little with temperature.

Figure 1.9a–c depicts the temperature-dependent changes in the FIR intensity of nylon-6 at (a) 294, (b) 222, and (c) 111 cm^{-1} from 22 to 210 °C [57d]. The intensity of the FIR band at 111 cm^{-1} did not change until approximately 60 °C, which corresponds to the glass transition of nylon-6 at approximately 54 °C. Above about 60 °C, the intensity decreased linearly and became constant at temperatures above approximately 170 °C. This temperature is close to the Brill transition of nylon-6 at 160 °C.

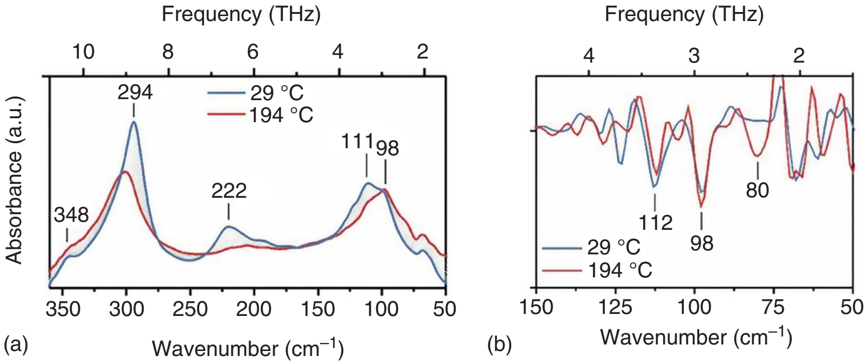

Figure 1.8 (a) FIR spectra of nylon-6 in the α-form measured from 29 to 194 °C and (b) their second derivatives at 29 to 194 °C. Source: Yamamoto et al. [57d].

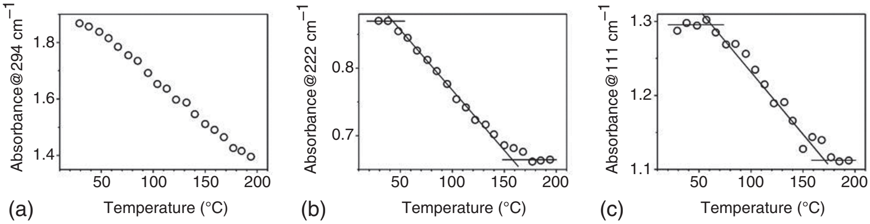

Figure 1.9 Temperature dependence of the FIR intensity of nylon-6 at (a) 294, (b) 222, and (c) 111 cm^{-1} from 22 to 210 °C. Lines are eye guides. Source: Yamamoto et al. [57d].

It is known that after the glass transition, the lattice lengths of the *a*- and *c*-axes of the α-form of nylon-6 gradually approach each other and finally reach unity after the Brill transition. This trend is similar to that of the FIR intensity at 111 cm^{-1}. Hence, the intensity at 111 cm^{-1} may be used as an indicator of the lattice length of nylon-6 in the α-form.

The intensity of the weak bands in the 240 to 190 cm^{-1} region decreased with temperature in a similar manner to that of the band at 111 cm^{-1}. The temperature dependence of the intensity at 222 cm^{-1} (Figure 1.9b) yields transition temperatures of c. 50 °C (glass) and 160 °C (Brill). The intense band at 294 cm^{-1} became weaker and broader with increasing temperature; however, the peak top intensity only gradually decreased and did not show any clear transition (Figure 1.9a).

Figure 1.10 shows (a) the Raman spectra of nylon-6 in the α-form in the 180 to 70 cm^{-1} region at 22, 90, 150, and 210 °C and (b) their second derivatives at 22–150 °C [57d]. In the Raman spectrum obtained at 22 °C, a broad and strong Raman peak was observed at 104 cm^{-1}. On increasing the temperature to 150 °C, the maximum peak position shifted to 100 cm^{-1}. The second-derivative spectra (Figure 1.10b) reveal that this shift is induced by a relative change in the intensities of the two peaks.

Figure 1.11 presents (a) the polarized Raman and (b) FIR spectra of nylon-6 in the α-form at room temperature with polarization perpendicular (red lines) and parallel (black lines) to the stretched direction of the nylon film [57d]. Both the strong

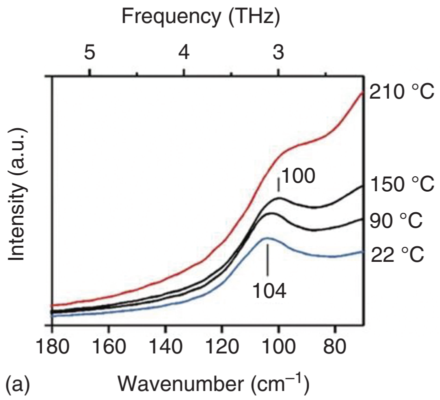

Figure 1.10 (a) Raman spectra of nylon-6 in the α-form collected at 22, 90, 150, and 210 °C and (b) their second derivatives at 22–210 °C. Source: Yamamoto et al. [57d].

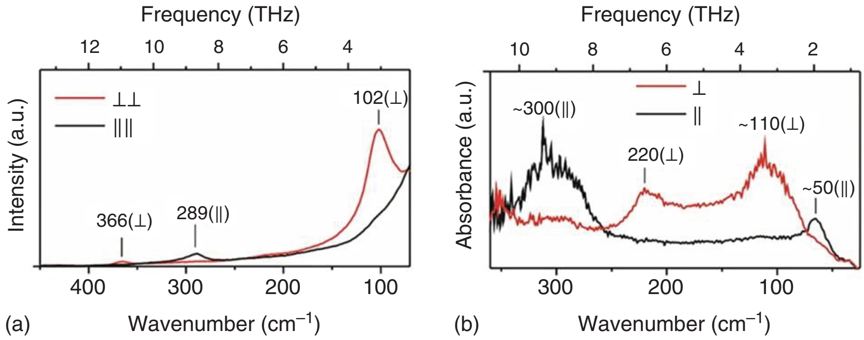

Figure 1.11 (a) Polarized Raman and (b) FIR spectra of nylon-6 in the α-form at room temperature with polarization perpendicular (red lines) and parallel (black lines) to the stretched direction of the nylon film. Source: Yamamoto et al. [57d].

Raman band at approximately 102 cm^{-1} and FIR band at approximately 110 cm^{-1} are polarized perpendicular to the chain axis, suggesting correspondence of these two bands. Comparisons of the experimental (top) and calculated (bottom) (a) Raman and (b) FIR spectra of crystalline nylon-6 in α-form are shown in Figure 1.12 [57d]. The calculations were carried out using the fragment methodology at the CAM-B3LYP-GD3BJ/6-311++G** level of theory. On the basis of the peak positions and polarization directions, the calculated bands at 365, 273, and approximately 210 cm^{-1} were ascribed to experimental Raman bands at 365, 289, and 213 cm^{-1}, respectively. In the lower wavenumber region, perpendicularly polarized strong Raman bands were calculated at 127, 108, and 89 cm^{-1}. It is very likely that the calculated strongest band at 108 cm^{-1} corresponds to the experimental band at 104 cm^{-1}.

The agreement of the FIR spectra was also satisfactory in terms of the band positions, spectral shapes, and polarization directions. The FIR bands at 294 and 222 cm^{-1} were calculated to be 274 and 216 cm^{-1}, respectively, consistent with

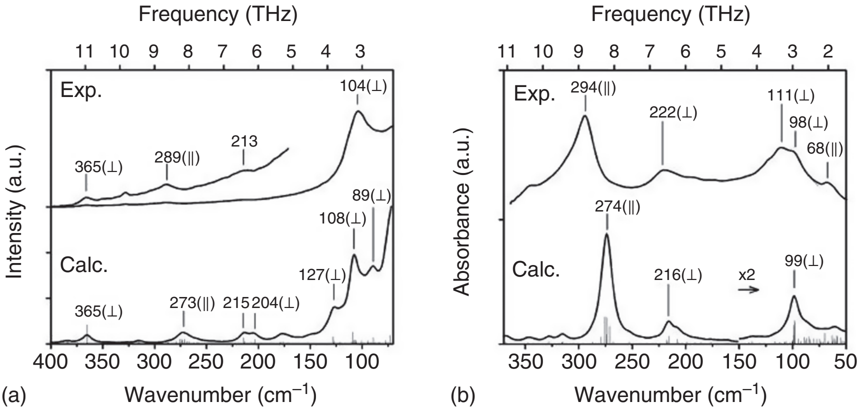

Figure 1.12 Comparisons of the experimental (top) and calculated (bottom) (a) Raman and (b) FIR spectra of crystalline nylon-6 in the α-form. The calculations were carried out using the fragment methodology at the CAM-B3LYP-GD3BJ/6-311++G** level of theory. Polarization directions are indicated as parallel (||) or perpendicular (⊥) to the chain axis of nylon-6. The calculated FIR intensity below 150 cm^{-1} is doubled for clarity. Source: Yamamoto et al. [57d].

the polarization directions. In the lower-wavenumber region of the calculated spectrum, one can find an FIR band at 99 cm^{-1} showing perpendicular polarization and a weak shoulder at approximately 80 cm^{-1}. These calculated bands were ascribed to the experimental bands at approximately 111 and 98 cm^{-1} based on the polarization and intensities.

Figure 1.13 illustrates the atomic motion corresponding to the FIR active modes of nylon-6 at (a) 247, (b) 216, and (c) 99 cm^{-1} viewed from the origin of the a-axis [57d]. The two chains along the a-axis are overlapped in this figure, and the bold letters in (c) indicate atoms in the front chains. The calculated atomic motions corresponding to the FIR band at 99 cm^{-1} (Figure 1.13c) are a mixture of the torsional motion of the methylene groups and the transverse mode of amide groups, in which the NH and O atoms oscillate out of the amide plane. This assignment is partly in agreement with the previous one based on the normal-mode analysis [70, 71], which is the torsional motion of the methylene chain. However, Yamamoto et al. [57d] found that amide groups also contributed to this mode. As discussed later, the amide groups govern the intensity of the FIR band. Our own calculations indicate that the translational motion of the amide groups is not involved in this mode, although its involvement has been reported [72]. As discussed above (Figure 1.9c), the temperature dependence of the FIR intensity at 111 cm^{-1} yielded two transition points corresponding to glass and Brill transitions. The torsional nature of this band can explain why the intensity is sensitive to changes in the lattice length. The calculated Raman band at 108 cm^{-1} has similar atomic motions to the FIR band at 99 cm^{-1}: the torsion of methylene groups and the transverse motion of the amide groups.

Figure 1.14 shows the simulated (a) Raman and (b) FIR spectra of nylon-6 in the α-form with atomic tensors of amide groups zeroed out (red) and exact (black) [57d]. Notably, except for the Raman band at 270 cm^{-1}, the intensities of all the other

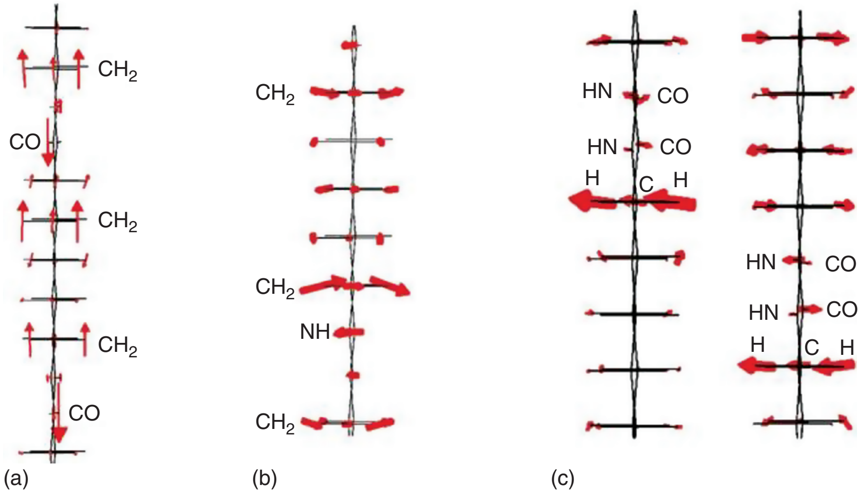

Figure 1.13 Atomic motion of the FIR active modes of nylon-6 in the α-form calculated at (a) 247, (b) 216, and (c) 99 cm^{-1} viewed from the origin of the *a*-axis. Two chains along the *a*-axis are overlapped in this figure, and the bold letter in (c) indicates atoms in the front chains. Source: Yamamoto et al. [57d].

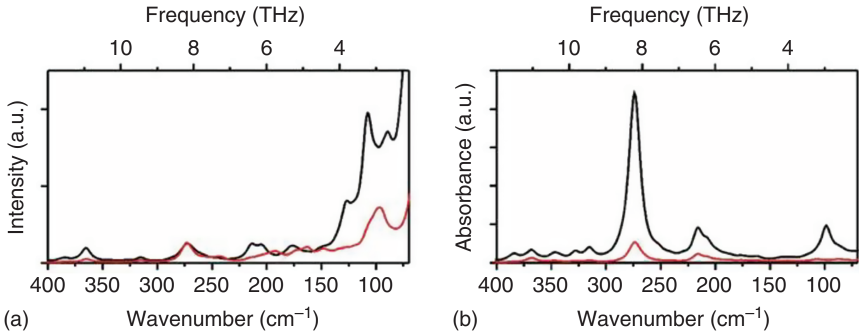

Figure 1.14 Calculated (a) Raman and (b) FIR spectra of nylon-6 in the α-form with atomic tensors of amide groups zeroed out (red) and exact (black). Source: Yamamoto et al. [57d].

major Raman and FIR bands are decreased markedly by zeroing out. These results indicate the dominant contribution of the amide groups to the low-frequency intensities. In particular, the FIR bands at approximately 100 cm^{-1} were nearly perfectly erased, suggesting that the FIR band is highly sensitive to the chemical environment of the amides. Interestingly, the atomic motions corresponding to the FIR band at 99 cm^{-1} were dominated by the methylene group, but their absorption intensity was governed by the amide groups. These calculation results indicate that the experimentally observed decrease in absorption at 111 cm^{-1} with increasing temperature is a result of changes in the chemical environment of the amide groups during the change in crystal lattice length. In contrast, the corresponding Raman intensity at about 108 cm^{-1} is derived not only from the amide groups but also from the methylene part.

1.3.3 NIR Spectra of Linear Low-Density Polyethylene and Their Chemometrics Analysis

NIR spectroscopy has been used not only for basic studies of polymers, such as hydrogen bonding, intermolecular interactions, and physical properties, but also for practical applications [15–17]. Several examples of both can be found in Chapter 5. However, here, we present one particularly good example of an application: a combined chemometrics and spectral pretreatment method yielding band assignments based on loading plots of PCA and partial least squares (PLS) analysis [73]. NIR DR spectra were measured for pellets of 16 types of linear low-density polyethylene (LLDPE) with short branches and polyethylene (PE) to enable band assignment and build calibration models that predict their density [73]. The density of the LLDPE samples was in the range of 0.911–0.925 g cm^{-3}. The original NIR spectra data set, their second derivatives, and the spectra after multiplicative scatter correction (MSC) treatment were used to develop the models. The correlation coefficients were calculated to be 0.961, 0.965, and 0.970 for the original NIR spectra, their second derivatives, and those with the MSC treatment, respectively, and the standard error of prediction (SEP) was found to be 0.001 g cm^{-3} for all cases. It was found from the regression coefficient (RC) plots for the calibration models that bands at 1192, 1376, and 1698 nm originating from the overtone and combination modes of the CH_3 groups contribute significantly to the density prediction [73].

Figure 1.15 compares the NIR DR spectrum of one of the LLDPE samples with that of PE [73]. As shown in Figure 1.15, the NIR spectrum of LLDPE with short branches is significantly different from that of PE without a branch. For example, PE showed intense bands at 1728 and 1764 cm^{-1}. The band assignments were not straightforward; however, based on previous NIR studies on alkyl compounds and polymers, Shimoyama et al. [73] assigned bands in the 1140–1250 nm region to the second overtones of CH_2 stretching modes or their combination modes: specifically, those in the 1350–1450 nm region to the combinations of 2 × C–H stretch (str) + C–H deformation (def) (CH_2 or CH_3), and those in the 1700–1800 nm region to the first overtones of CH_2 stretching modes or their combination modes. They assigned bands at 1146, 1186, 1374, 1644, and 1698 nm to CH_3 group vibrations, as will be discussed later. PE shows two characteristic features in the 1720–1770 nm region, originating from the CH_2 vibrational modes. It should be noted that the bands arising from the CH_2 groups are relatively stronger in the spectrum of PE, whereas those arising from the CH_3 groups are more prominent in the spectrum of LLDPE.

Figure 1.16a,b shows the NIR spectra of the 16 types of LLDPE and PE before and after MSC treatment, respectively. Notably, the baseline varies from one sample to another for the pellet samples, and the MSC treatment is useful for baseline correction [73]. The second derivatives of the NIR spectra shown in Figure 1.16a are presented in Figure 1.17. The second derivative spectra identified weak bands at 1146, 1186, 1300, 1374, 1634, 1696, and 1730 nm, which are not always clearly observed in the original spectra. The second derivative spectra clearly differentiate the spectra of LLDPE from that of PE in the 1160–1220, 1360–1400, and 1630–1780 nm regions.

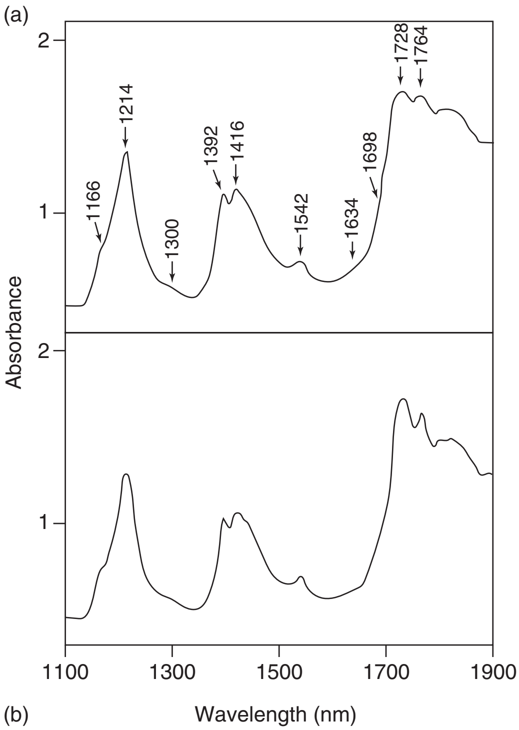

Figure 1.15 (a) A NIR DR spectrum of LLDPE sample and (b) that of PE. Source: Shimoyama et al. [73].

Figure 1.18 displays a score plot of PCA factors 1 and 2 for 51 MSC-pretreated NIR spectra in the 1100–1900 nm region of the 16 types of LLDPE and PE (NIR spectra were measured three times for each polymer) [73]. The NIR spectrum of PE was clearly discriminated from the rest using two factors. The polycarbonate (PC) weight-loading plot of factor 1 for the score plot shown in Figure 1.18 is presented in Figure 1.19 [73]. The loading has three upward peaks at 1192, 1380, and 1698 nm and three downward peaks at 1542, 1728, and 1764 nm. Shimoyama et al. [73] ascribed the upward peaks to the overtone or combination modes of the CH_3 groups and the downward peaks to those of the CH_2 groups. Notably, the bands at 1192, 1380, and 1698 nm are very weak or almost missing in the raw spectra in Figures 1.15 and 1.16, but they play key roles in the discrimination of PE and the LLDPEs. Thus, it is very likely that factor 1 reflects the existing ratio of the number of CH_3 and CH_2 groups.

Shimoyama et al. [73] developed a PLS regression calibration model to predict the density of LLDPE using their MSC-treated NIR spectra. It was found from the plot of the residual validation variance of the PLS regression that four factors were sufficient for prediction. They attempted to build principal component regression (PCR) and PLS regression calibration models based on the raw spectra, their second derivatives, and the spectra after MSC treatment. The PLS regression analysis yielded significantly better results than the PCR analysis, and, among the PLS results, the MSC treatment gave somewhat better results than the second derivative.

A loading plot of the RCs for the model obtained from the NIR spectra after MSC is depicted in Figure 1.20 [73]. The RC plot is characterized by three downward peaks

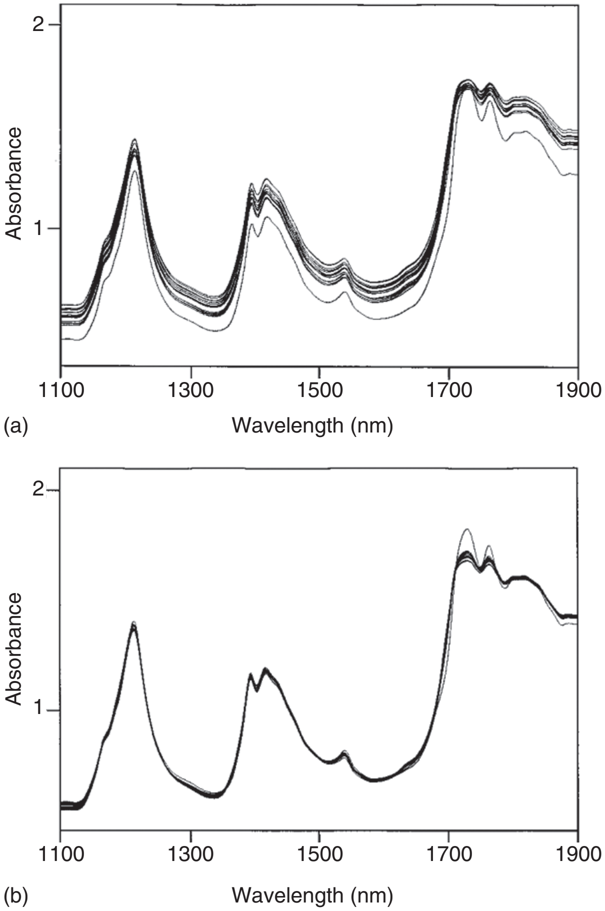

Figure 1.16 NIR spectra of the 16 kinds of LLDPE and PE investigated (a) before and (b) after MSC treatment. Source: Shimoyama et al. [73].

at 1192, 1376, and 1698 nm arising from the CH_3 groups. These bands are not clear in the raw spectra but are prominent in the RC plot. An upward peak at 1542 nm corresponds to the band derived from the CH_2 groups. As shown in Figure 1.20, the RC plot is related to the relative intensities of the CH_3 and CH_2 bands. The density of LLDPE is controlled by the number and types of branches attached to the main chain of the PE. The lower the density, the larger the number of CH_3 groups. Therefore, it seems reasonable that NIR spectroscopy can predict the density of LLDPE in terms of the number of CH_3 groups.

1.3.4 Study of the Crystallization Behavior of Asymmetric PLLA/PDLA Blend by IR and Raman Spectroscopy and Raman Imaging

In this study, the isothermal crystallization of an asymmetric poly(L-lactide)/poly(D-lactide) (PLLA/PDLA) blend (4/1) at around 100 °C was investigated by IR,

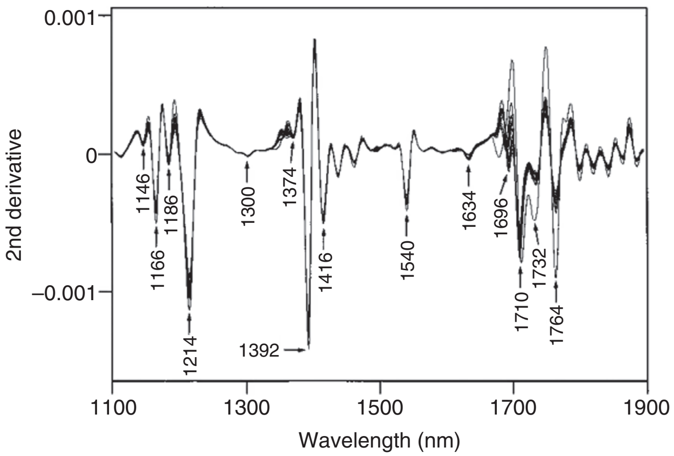

Figure 1.17 Second derivative of the NIR spectra shown in Figure 1.16a. Source: Shimoyama et al. [73].

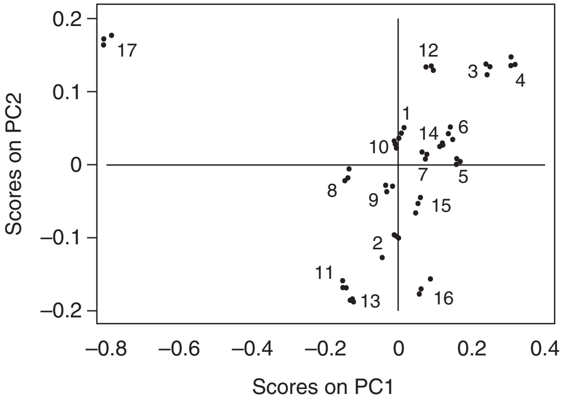

Figure 1.18 Score plot of PCA factors 1 and 2 for the 16 kinds of LLDPE and PE based on 51 NIR spectra recorded in the 1100–1900 nm region (NIR spectral data were pretreated by MSC). The numerals adjacent to each point indicate the sample number. Source: Shimoyama et al. [73].

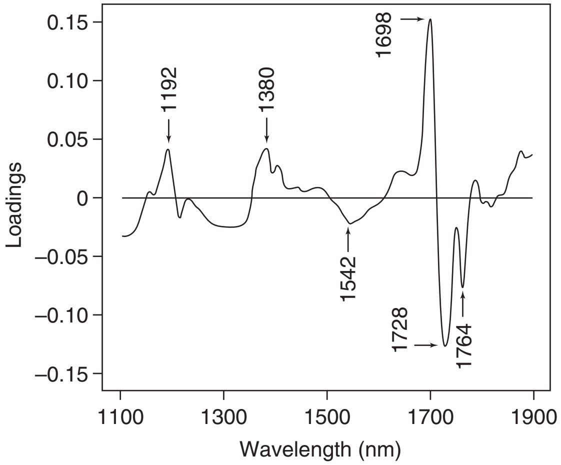

Figure 1.19 A PC weight-loadings plot of factor 1 for the score plot shown in Figure 1.18. Source: Shimoyama et al. [73].

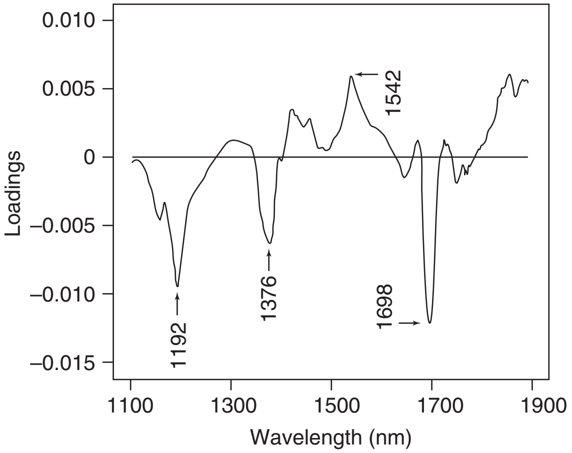

Figure 1.20 Loadings plot of regression coefficients for the PLS calibration model from the MSC treated NIR spectra. Source: Shimoyama et al. [73].

Raman, and Raman imaging [74]. The IR results indicate that the crystallization of the homocrystal (HC) of the blend was delayed owing to the formation of a large amount of the stereocomplex (SC) in the isothermal process. A unique spherulite morphology was observed through polarized optical microscopy (POM), and the distributions of SC and HC in and out of the large spherulites were revealed by Raman imaging measurements. These results demonstrate that the SC crystals are homogeneously dispersed in both the AMP and spherulite regions. In contrast, the HC crystal was located mainly in the large spherulite area. A possible isothermal crystallization process for an asymmetric PLLA/PDLA blend was proposed.

Figure 1.21 shows the time-dependent variations in the IR spectra in the 970 to 890 cm^{-1} region of asymmetric PLLA/PDLA 4/1 blend collected during the isothermal crystallization process at 100 °C [74]. Formation of both SC and HC poly(lactic acid) (PLA) was found in the C–C stretching region. It was reported that the band at 908 cm^{-1} is due to the 3/1 helix conformation in PLA SC crystal lattice, whereas the band at 921 cm^{-1} derives from the 10/3 helix conformation, which exists in the PLA α'/α HC [74]. As shown in Figure 1.22, the band at 908 cm^{-1} appears before that at 921 cm^{-1}, indicating that the SC appears first at the isothermal temperature of 100 °C [74]. Thus, clearly, their crystallization rates and completing times are asynchronous.

Figure 1.23a–c displays POM images of the asymmetric blend sample of PLLA/PDLA (4 : 1) isothermally crystallized at 100 °C for different times [74]. As shown in Figure 1.23a–c, the growth of spherulites starts from the inside to the outside and may consist of many small crystallite domains. Figure 1.23d shows the round shape of a large spherulite observed from the melt, and Figure 1.23e shows the result of the crystallization of a neat PLLA HC at the same temperature (100 °C). As shown in Figure 1.23d, a light circle corresponding to a spherulite was observed with a radius of approximately 50 μm. However, a black Maltese cross was not observed, in contrast to the HC of neat PLLA under the same crystallization conditions (Figure 1.23d). To provide new insights into the composition, Zhang et al. conducted Raman imaging experiments.

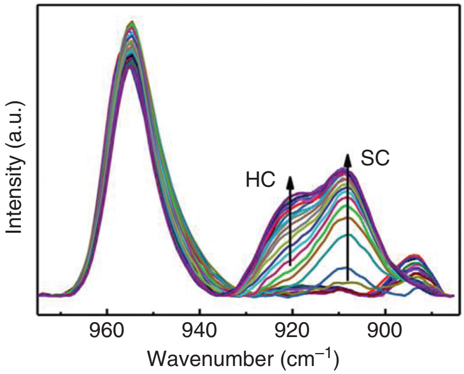

Figure 1.21 Time-dependent IR spectra of asymmetric PLLA/PDLA 4/1 blend, which were measured in the isothermal crystallization process at 100 °C. Source: Hu et al. [74].

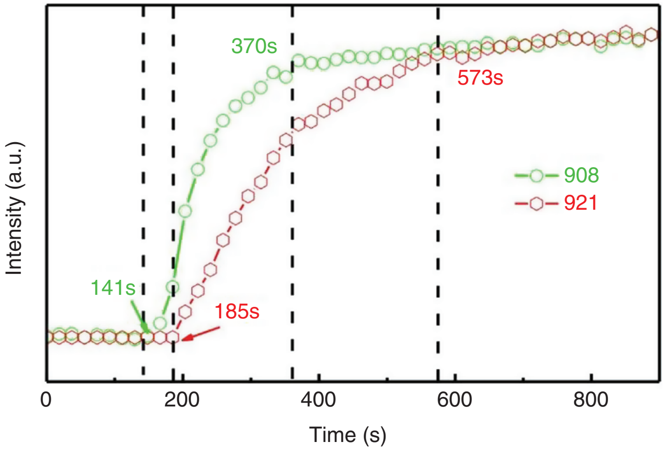

Figure 1.22 Time-dependent variations of IR band intensity of SC at 908 cm^{-1} and that of HC at 921 cm^{-1} at an isothermal temperature of 100 °C. Source: Hu et al. [74].

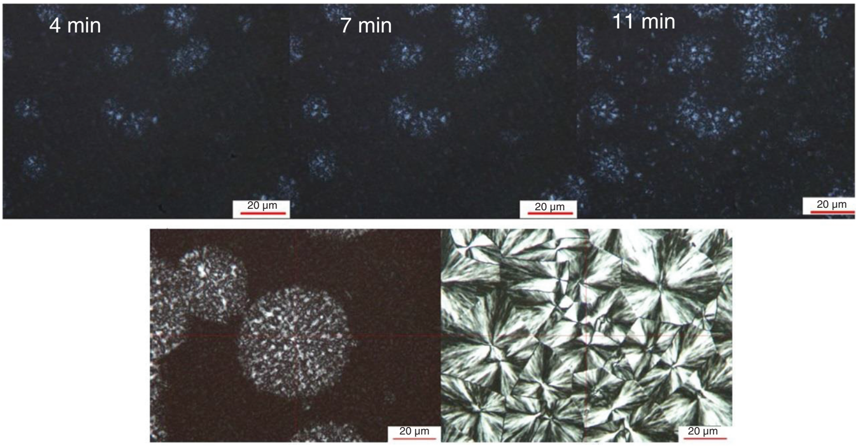

Figure 1.23 POM images of the asymmetric blend sample of PLLA/PDLA (4 : 1) collected at a melt-isothermal temperature of 100 °C for (a) 4, (b) 7, and (c) 11 mm; (d) whole spherulite morphology and (e) PLLA spherulite morphology obtained at an isothermal temperature of 100 °C. Source: Hu et al. [74].

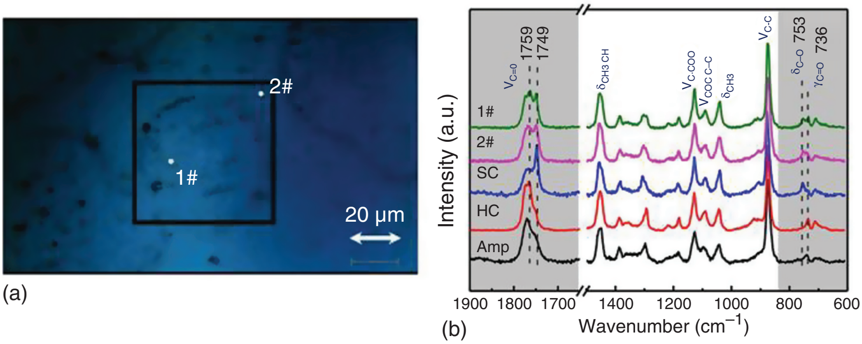

Figure 1.24 (a) Optical image of the blend sample after isothermal crystallization at 100 °C for 15 minutes (black framed region is the imaging region). (b) Raman spectra measured at different positions and those of PLA different crystal forms; #1: point located within the spherulite region, #2: point out of the spherulite, SC: stereocomplex 1 : 1 PLLA/PDLA blend isothermal crystallization at 200 °C, HC: Homocrystal PLLA isothermal at 100 °C, Amp: amorphous PLLA quenched sample from melting. Source: Hu et al. [74].

Single-point Raman measurements focusing on the large spherulite region were carried out first. Figure 1.24a shows an optical image of the blend sample after isothermal crystallization at 100 °C for 15 minutes (the black framed region is the imaging region) [74]. Figure 1.24b shows the Raman spectra collected at different positions marked in #1 and #2 in Figure 1.24a. The Raman spectra of SC, HC, and AMP PLA measured at different states are also shown in the same figure. Examining the whole Raman spectra, the five spectra in Figure 1.24b are very similar to each other; however, there are significant differences in the $\nu C=O$ (1800 to 1700 cm^{-1}) and $\gamma C=O/\delta C—O$ (800 to 700 cm^{-1}) regions. In the former region, the spectrum of the #1 point is similar to that of #2, and they are distinctly different from the spectrum of SC. HC and Amp yielded similar spectra in this region. In the region from 800 to 700 cm^{-1}, the relative intensities of the bands at 733 and 755 cm^{-1} could be used to distinguish SC from HC.

Zhang and coworkers [74] developed Raman images using both the 1800 to 1700 and 800 to 650 cm^{-1} regions. Here, we explain the results for the images based on the 800 to 650 cm^{-1} region. Figure 1.25a shows the Raman spectra and their curve-fitting results in the 800 to 650 cm^{-1} region measured at points #1 and #2, and Figure 1.25b presents Raman spectra in the same region of PLA SC, HC, and AMP with curve-fitting results [74]. As shown in Figure 1.25b, there are specific bands for HC and SC at 736 and 754 cm^{-1}, respectively. Images constructed using the band intensities at 754 and 736 cm^{-1} are displayed in Figure 1.25c,d, respectively. Figure 1.25c illustrates the intensity distribution of the band at 754 cm^{-1} based on the curve-fitting result shown in Figure 1.25a. As shown in Figure 1.25d, the spherulite region had the highest intensity for the band at 736 cm^{-1}. Combined with the discussion above, Zhang and coworkers [74] concluded that the SC disperses everywhere in the sample, whereas HC mainly exists within the large spherulite region.

In summary, the IR results reveal that the formation of the SC occurred prior to that of the HC during the isothermal process. POM measurements indicated that

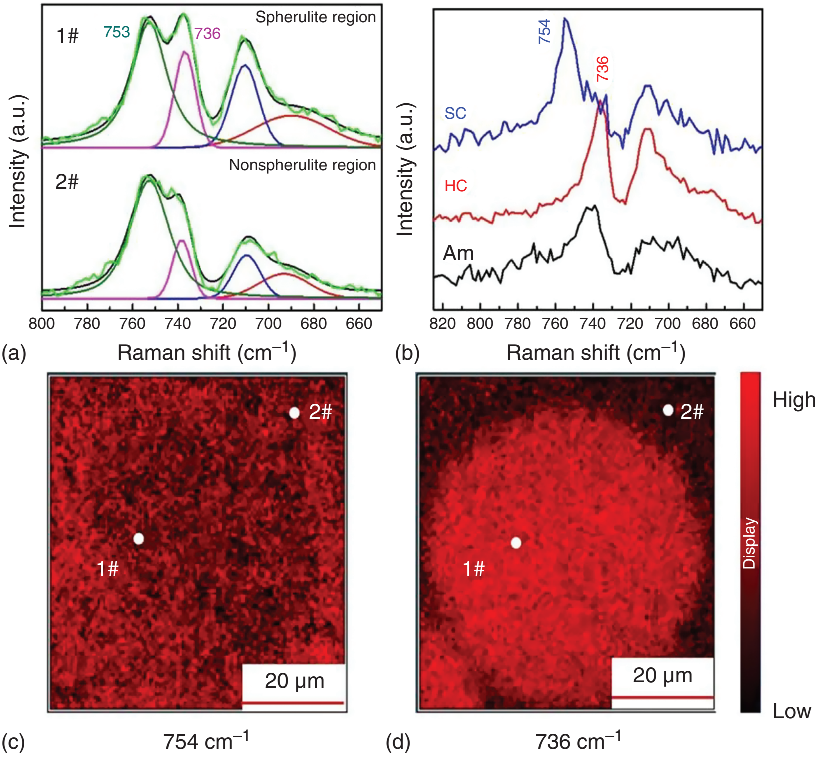

Figure 1.25 (a) Curve-fitting results in the 800 to 600 cm^{-1} region at single points (positions #1 and #2) and (b) Raman spectra of SC, HC, and Amp of PLA; (c, d) Raman images developed using the band intensities at (c) 754 and (d) 736 cm^{-1}. Source: Hu et al. [74].

large spherulites appeared after the formation of small crystallites. However, the crystallization of HC does not correspond to the already-formed SC crystals. This observation is unlike the normal case in which crystals exclude other components from their own domains. Based on the above discussion, Zhang and coworkers [74] proposed a possible crystallization process for the asymmetric PLA sample, as shown in Figure 1.26. In the first step, owing to the strong hydrogen-bonding interaction between PLLA and PDLA, the nucleation of the SC occurs much more easily than that of the HC phase. Considering chain entanglement, it is very likely that the already-formed SC acts as a crosslinking point, which may restrict the mobility of the PLLA chain. Next, the superfluous PLLA chains are excluded from the SC domains and start to crystallize on the surface of the SC domains. Finally, the SC and HC crystals grow together to form large spherulites.

1.3.5 3D SERS Imaging Using Chemically Synthesized Highly Symmetric Nanoporous Silver Microparticles

Recently, 3D SERS substrates have been developed by many research groups and have been shown to possess promising signal quality owing to their exponentially

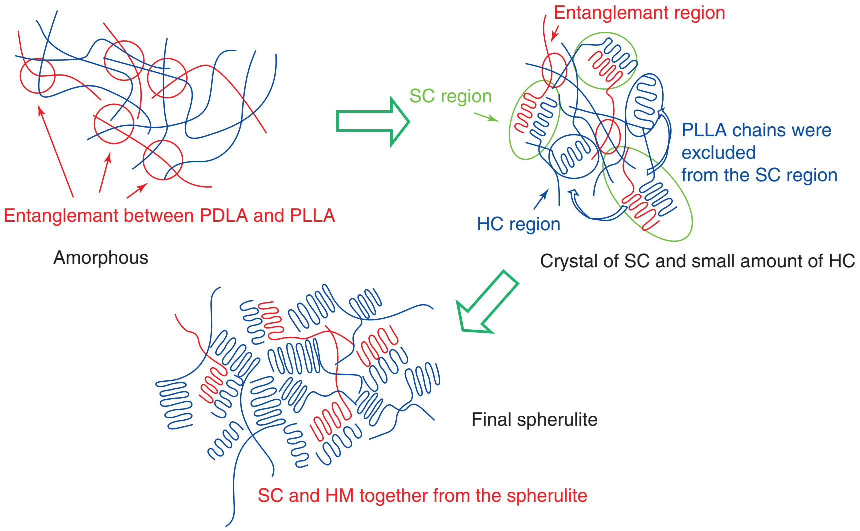

Figure 1.26 Schematic illustrations of isothermal crystallization process of PLLA/PDLA asymmetric blend. Source: Hu et al. [74].

large surface area and substantial number of hotspots from the additional third dimension. However, almost all 3D SERS substrate studies only present point-by-point measurements or 2D SERS imaging, which does not fully utilize the 3D nature of the substrates.

Vantasin et al. [75] developed 3D SERS imaging using highly symmetric 3D silver microparticles as a SERS substrate. The synthesized nanoporous silver microparticles possess a regular hexapodal shape and octahedral symmetry, although the synthetic method is purely chemical (vide infra) and does not involve lithography. The 3D SERS method was applied to detect the 3D inhomogeneity in a polymer blend, which relies on the predictable enhancement pattern of the substrate. 3D SERS imaging using the substrate also provides an improvement in spatial resolution along the *z*-axis, which is a challenge for Raman measurements in polymers, especially layered polymeric systems.

The nanoporous silver microstructures in this study were synthesized by the in-place galvanic reduction of an AgCl template. Figure 1.27a shows SEM images of nanoporous silver microstructures, showing the overall hexapod shape (scale bar: 5 mm). The nanopores, which act as hotspots, are shown in Figure 1.27b, having an average pore size of approximately 60 nm. With this pore size, small molecules such as SERS probe molecules can travel deep inside the cavities of the particles.

Figure 1.28a shows the SERS spectrum of *p*-aminothiophenol (PATP) from the center of the particle in Figure 1.28b. The band at 1074 cm^{-1} in the figure is assigned to the a_1 mode C–S stretching of PATP, which belongs to the C_{2v} point group. Figure 1.28c–e shows 3D SERS images developed using the peak area of the C–S stretching band. The enhancement pattern can be easily predicted because the top-view enhancement mapping in Figure 1.28c is very similar to the particle shape

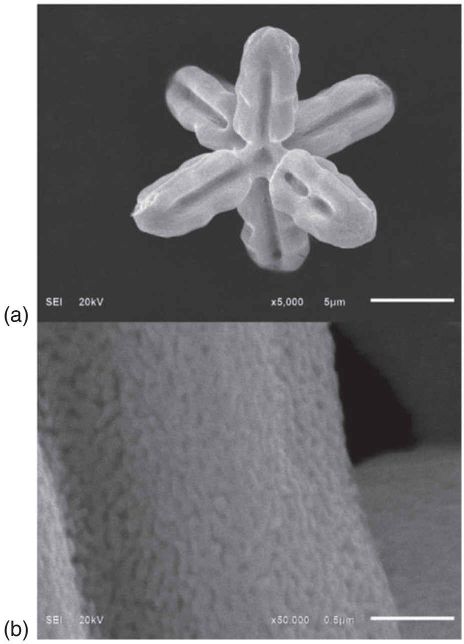

Figure 1.27 SEM images of nanoporous silver microstructures showing (a) the overall hexapodal shape (scale bar: 5 mm) and (b) the nanopores (scale bar: 0.5 mm). Source: Vantasin et al. [75].

in Figure 1.28b. The *xy*-slices shown in Figure 1.28e display an obvious pattern, as the hotspots gradually move from the upper leg positions to the lower leg positions.

A possible application of this 3D substrate was demonstrated by embedding the microparticles into polymers. In this experiment, a 1 : 1 blend of poly(3-hydroxybutyrate) (PHB) and poly(D,L)lactic acid (PDLLA) was used. Owing to the presence of the same functional groups, the interaction between each polymer and silver microparticles should be very similar, and variations in the measured SERS spectra should originate from the polymer distribution.

Figure 1.29a,b shows optical image and a side-view scheme of a silver microparticle in a PHB/PDLLA polymer blend [75]. Figure 1.30c,d shows 3D SERS imaging of the particle based on ratio of the two bands at 870 and 840 cm^{-1} originating from the C–COO stretching modes of PDLLA and PHB, respectively, and 3D Raman imaging showed the same peak ratio, although for the polymer on the outside of the particle. Examples of 2D slices along the *z*-axis shown in Figure 1.30c,d are shown in Figure 1.30e,f, respectively. Only one in five slices (corresponding to 1.0 mm distance) is shown. For example, the upper legs of the silver hexapod in Figure 1.30a are located around 3 mm under the polymer surface, and the particle bottom is still several micrometers above the underlying glass slide (see Figure 1.30b).

The 3D image based on the peak area ratio shows a high value in some microscale areas, which could be interpreted as an inhomogeneity in the blend (in which the area consists of more PDLLA content). In fact, normal 3D Raman imaging can also be used to probe the inhomogeneity in polymers, but it is well known that conventional Raman spectroscopy in polymers suffers from a limitation in spatial resolution owing to the refraction of light at the polymer interface, especially in the *z*-axis,

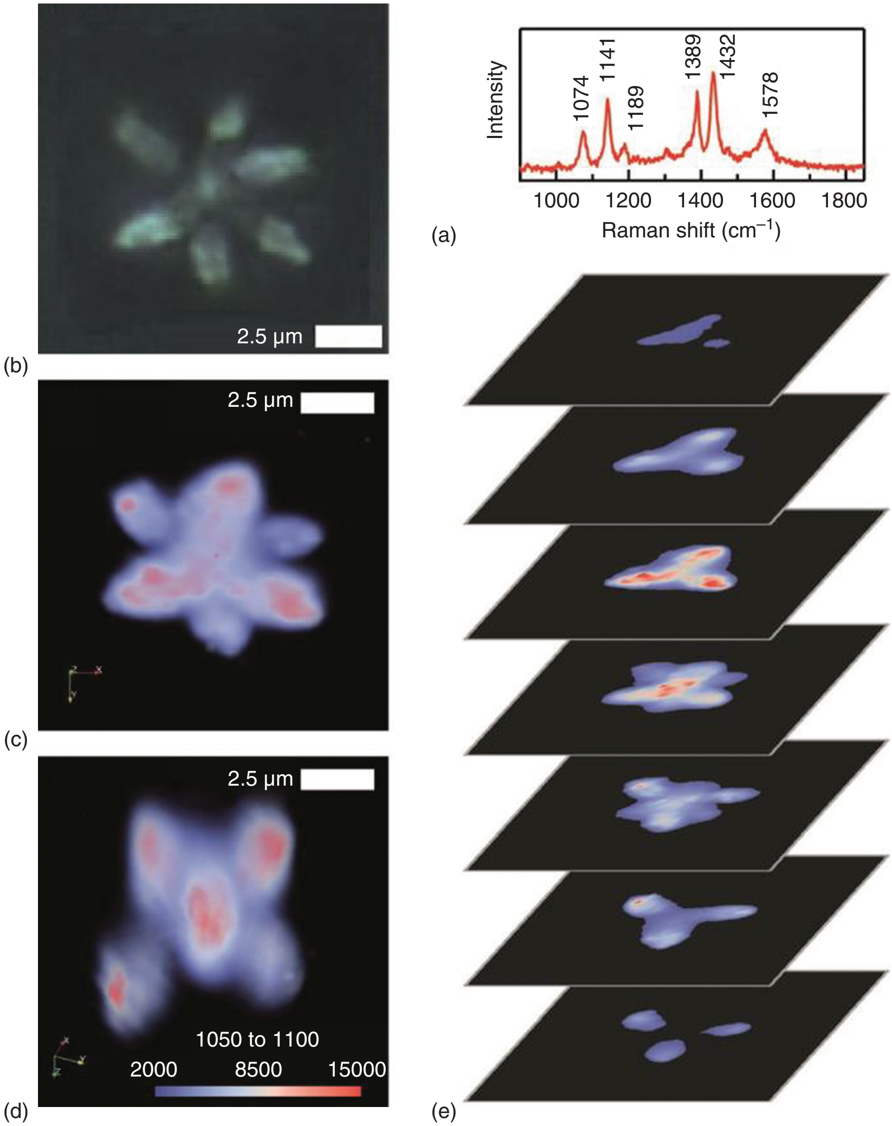

Figure 1.28 (a) SERS spectrum of PATP from the center of a hexapodal silver microstructure. (b) An optical microscopy image of the particle. (c, d) Top and diagonal views of 3D SERS images measured from the particle shown in (b) rendered using the peak area from the PATP a_1 mode at 1074 cm^{-1}. (e) Examples of 2D slices along the *z*-axis of (b). Only one in five slices (corresponding to a 1.5 mm distance) is shown. Note that (c), (d), and (e) use the same color scale. Source: Vantasin et al. [75].

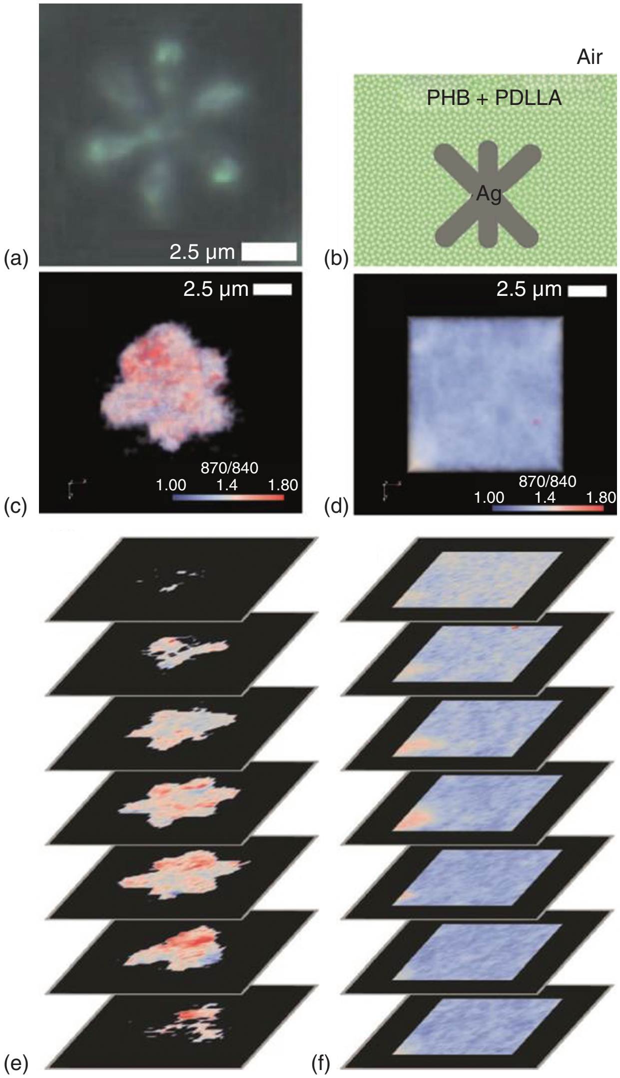

Figure 1.29 A silver microparticle in a PHB/PDLLA polymer blend. (a) An optical image. (b) A side-view scheme. (c) 3D SERS imaging on the particle showing the 870/840 cm^{-1} peak ratio. (d) 3D Raman imaging showing the same peak ratio but on the polymer outside of the particle. (e, f) Examples of 2D slices along the *z*-axis from (c) and (d), respectively. Only one in five slices (corresponding to 1.0 mm distance) is shown. Source: Vantasin et al. [75].

and this limit could be as low as 20 mm. As shown in the 3D Raman images of the nearby polymer without the silver structure (Figure 1.29d,f), the inhomogeneity is not resolved very well. This is due to the poor resolution in the *z*-axis, which causes the spectrum from every point to be similar to that of the bulk average. With the symmetric 3D SERS substrate, the probing volume for each measurement point is constrained to a smaller volume near the corresponding surface of the silver particle in the *z*-axis, thus improving the *z*-axis spatial resolution. Therefore, the microscale inhomogeneity can be resolved [75].

Double-layered polymeric systems were employed to demonstrate the potential of this method for improving the spatial resolution along the *z*-axis [75]. The hexapodal silver particles were embedded into the interface between polyvinylpyrrolidone (PVP) and polystyrene (PS; Figure 1.30a,b) [75] used the peak area ratio between the band arising from the PS ring-mode vibration at 1002 cm^{-1} and that arising from

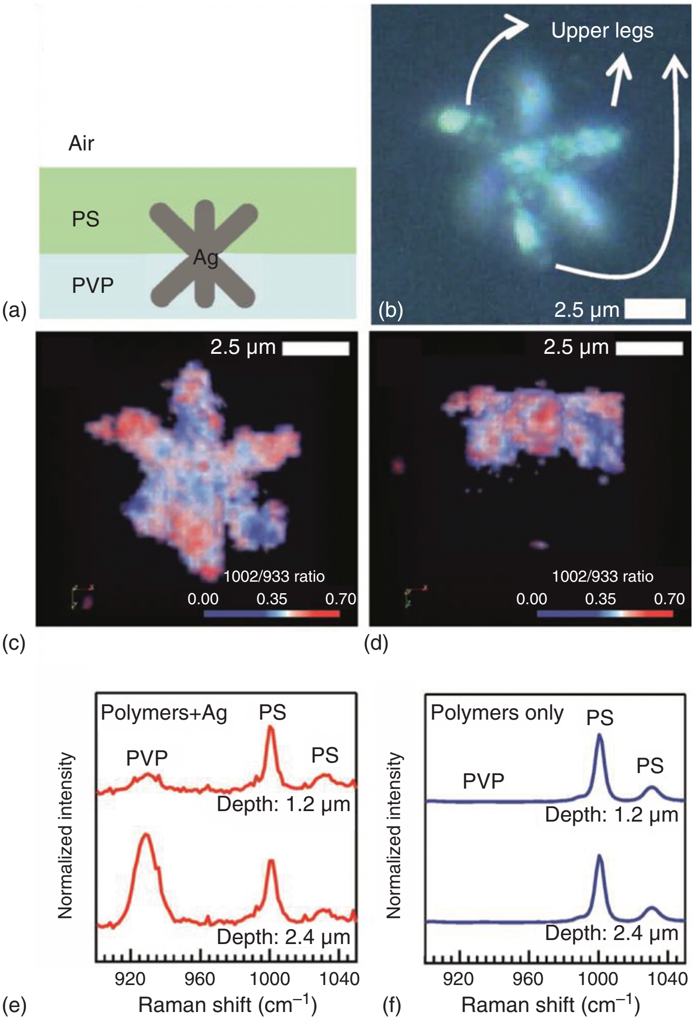

Figure 1.30 (a) Scheme showing a silver particle embedded in double-layered polymers. (b) An optical image of the silver particle in the polymers. (c, d) Top- and side-view 3D SERS images constructed from the peak area ratio between the 1002 cm^{-1} band of PS and the 933 cm^{-1} band of PVP. (e, f) Average spectra at depths 1.2 and 2.4 mm from 3D SERS imaging and normal 3D Raman imaging, respectively. Source: Vantasin et al. [75].

PVP C–C ring breathing at 933 cm^{-1} and clearly observed the partition of the polymers. The top- and side-view 3D SERS images in Figure 1.30c,d show high PS/PVP peak area ratios on the upper legs of the particle and low ratios on the lower legs. This cannot be replicated in normal 3D Raman imaging because the gradient of the peak area ratio is low. More quantitative information can be acquired by considering the averaged spectra at each depth. The particle appears flatter than normal in the side view (Figure 1.30d) because of the refraction (objects in a medium with a high refractive index have a smaller apparent height when viewed from above). Figure 1.30e,f clearly reveals that the contrast between the 1.2- and 2.4-mm depths in 3D SERS imaging is much better than that in normal 3D Raman imaging. However, this resolution improvement in the z-axis overcomes the limitation of refraction at polymer interfaces, and it does not exceed the diffraction limit of light, which is approximately 580 nm in the PS with this setup.

Thus, using 3D SERS imaging, Vantasin et al. [75] succeeded in characterizing highly symmetric nonporous silver microparticles for their SERS properties in three dimensions. The results demonstrate that the substrate can provide volumetric SERS information, and the enhancement pattern of the particles is very predictable because it correlates well with the particle shape. Further, a potential application of the embedded SERS probe was demonstrated: In a PHB/PDLLA polymer blend, 3D SERS imaging of this symmetric nonporous silver structure could resolve the microscale inhomogeneity of the blend. The improved spatial resolution along the z-axis was also illustrated in a double-layered polymeric system.

1.3.6 Tip-Enhanced Raman Scattering Spectroscopy Study of Local Interactions at the Interface of Styrene–Butadiene Rubber/Multiwalled Carbon Nanotube Nanocomposites

This is an example of a TERS study of polymer nanocomposites [76]. TERS is very useful for exploring the structure of nanomaterials [9, 33]. Local molecular interactions at the interface of styrene–butadiene rubber (SBR)/multiwalled carbon nanotube (MWCNTs) nanocomposites in films were explored using TERS spectroscopy [76] (see Figure 1.31 for the structure of SBR). The TERS study revealed that the TERS peaks arising from the phenyl group of SBR were strong when the MWCNT bands were strong, whereas the vinyl-group bands of SBR were strong when the MWCNT bands were weak. These observations indicate that the local distribution

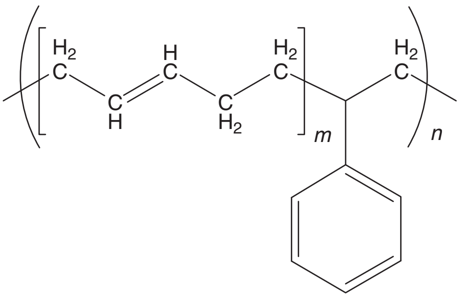

Figure 1.31 Chemical structure of SBR.

of polymer chains is modified by changes in the orientation of the phenyl rings by π–π interactions between the polymer chains and the MWCNTs.

Bokobza investigated SBR polymer nanocomposites containing MWCNTs and carbon black using Raman spectroscopy and discussed the dispersion of the fillers [77]. While this study is important, it could not provide new insights into local molecular interactions at the interface of SBR/MWCNT nanocomposites. Therefore, Suzuki et al. investigated the local molecular interactions at the interface using TERS. Figure 1.32a–c depicts the Raman spectra of pure SBR, pure MWCNTs, and a 1 wt% SBR/MWCNT nanocomposite, respectively [71]. Notably, the Raman spectrum of pure SBR is a normal Raman spectrum but that of pure MWCNTs is a resonance Raman spectrum and that of the 1 wt% SBR/MWCNT nanocomposite is a mixture of normal Raman and resonance Raman. One can easily assign bands at 2698, 1604, and 1354 cm^{-1} in the Raman spectrum of SBR/MWCNTs to G, G, and D bands, respectively (where G is the ordered carbon band and D is the disordered carbon band) of MWCNTs [76]. The Raman bands at 2990, 1668, and 1641 cm^{-1} in the same spectrum are due to the vinyl C–H stretching and *trans* and *cis* C=C stretching modes of SBR, respectively. The Raman bands at 3064 cm^{-1} and those at 1032 and 1004 cm^{-1} were derived from the aromatic C–H stretching and phenyl ring modes of SBR, respectively, and those at 2906 cm^{-1} arise from aliphatic C–H groups. Notably, the G band of SBR/MWCNT shifted to a higher wavenumber compared with that of the pure MWCNT spectrum. It is known that the shift of the

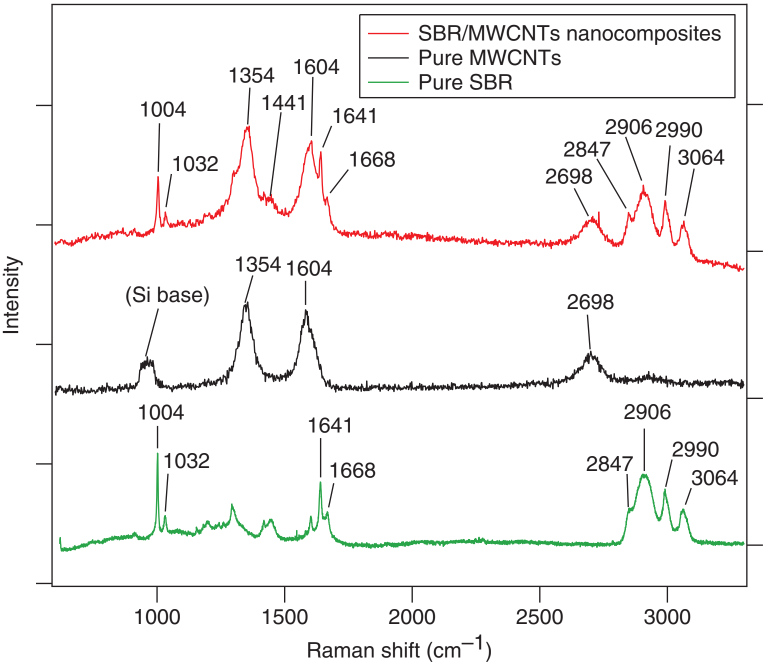

Figure 1.32 Raman spectra of (a) pure SBR, (b) pure MWCNTs, and (c) 1 parts per hundred rubber (phr) SBR/MWCNT nanocomposites. Source: Suzuki et al. [76].

G band in the Raman spectrum of carbon nanotubes (CNTs) is due to the shrinkage of the CNTs induced by the pressure from the polymer matrix [76].

The Raman and TERS spectra of 1 wt% SBR/MWCNT nanocomposite measured at the same eight points, positions (1), (2), (3), (4), (5), (6), (7), and (8), are compared in Figure 1.33a,b [76]. All Raman spectra in Figure 1.33a are similar. The TERS spectra collected at the eight points showed remarkable point-dependent changes. For example, in the spectrum obtained at position 7, the TERS signals assigned to SBR were identified at 2990, 2904, 2847, 1668, and 1641 cm^{-1}; however, the TERS signal at 1354 cm^{-1} arising from MWCNTs (D band) is considerably weaker than the corresponding peak in the Raman spectrum. Moreover, the G bands at 1604 and 2698 cm^{-1} were not observed in the spectrum collected at position 7. On the other

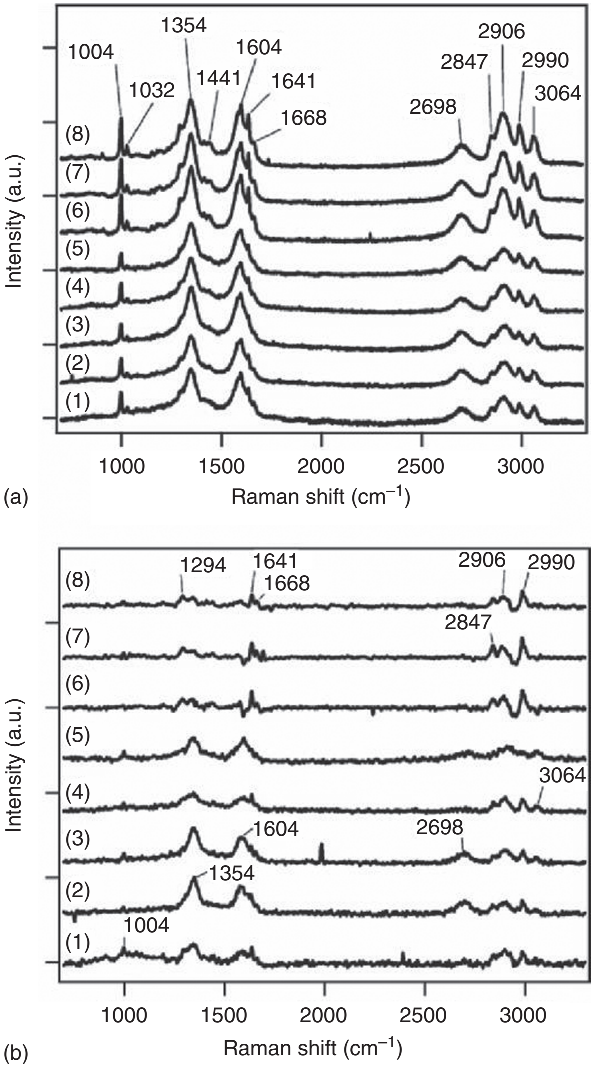

Figure 1.33 (a) Raman and (b) TERS spectra of 1 phr SBR/MWCNT nanocomposites measured at the eight points. Source: Suzuki et al. [76].

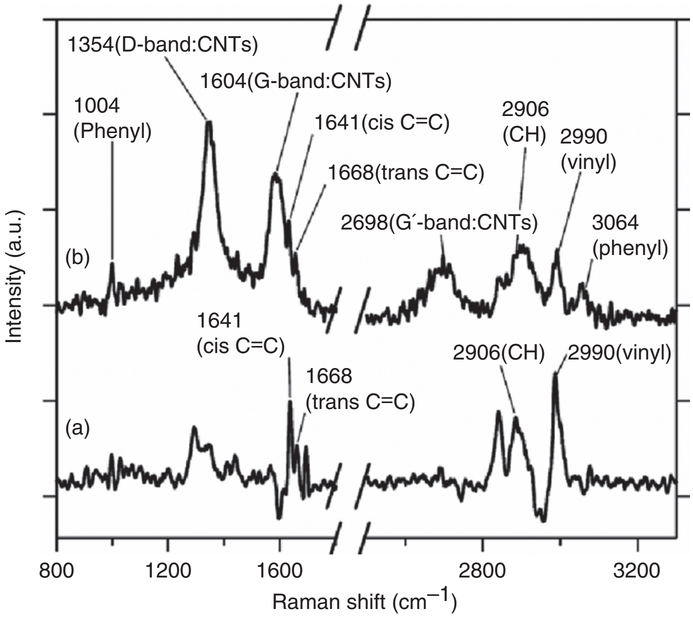

Figure 1.34 Enlarged TERS spectra of 1 phr SBR/MWCNTs from Figure 1.33: (a) spectrum 7 and (b) spectrum 3. Source: Suzuki et al. [76].

hand, in the TERS spectrum collected at position 3, signals originating from SBR were observed at 3064, 2990, 2904, and 2847 cm^{-1}, and those derived from MWCNTs were found at 2698, 1604, and 1354 cm^{-1}. The MWCNT content at 1 wt% was much lower than the polymer content in the sample. Hence, it is very likely that there are areas containing only SBR and those that include both SBR and MWCNTs. TERS measurements clearly detected their distribution.

Figure 1.34 shows the TERS spectra in the 1800 to 800 and 3200 to 2500 cm^{-1} regions measured at positions 7 and 3, respectively, in Figure 1.33b [76]. In the 3200 to 2500 cm^{-1} region, one can find four SBR peaks at 3064, 2990, 2906, and 2847 cm^{-1}. The former two peaks are assigned to CH (phenyl) and CH (vinyl) stretching modes, and the latter two peaks are antisymmetric and symmetric CH_2 stretching modes of the SBR chain, respectively. It is noted that in the TERS spectrum in Figure 1.34a, the signal at 3064 cm^{-1} is nearly absent, and the relative intensity of the signal at 2990 cm^{-1} became stronger than that of the corresponding signal in the spectrum in Figure 1.34a [76]. In Figure 1.34b, the TERS signals arising from MWCNTs appear strongly at 2698, 1604, and 1354 cm^{-1}, and a peak at 3064 cm^{-1} arising from aromatic C–H is clearly observed.

Figure 1.35 shows a plot of the intensities of the 3064 and 2990 cm^{-1} bands vs. that of the 1604 cm^{-1} band [76]. Figure 1.35a,b is related to the TERS data, whereas the data in Figure 1.35c,d are derived from the Raman spectra. As shown in Figure 1.35a,b, in the TERS spectrum (Figure 1.33b), the 2990 cm^{-1} signal (vinyl) decreases as the 1604 cm^{-1} signal (G band) increases, whereas the signal intensity at 3064 cm^{-1} (phenyl) increases as the G-band signal increase. In the Raman spectra

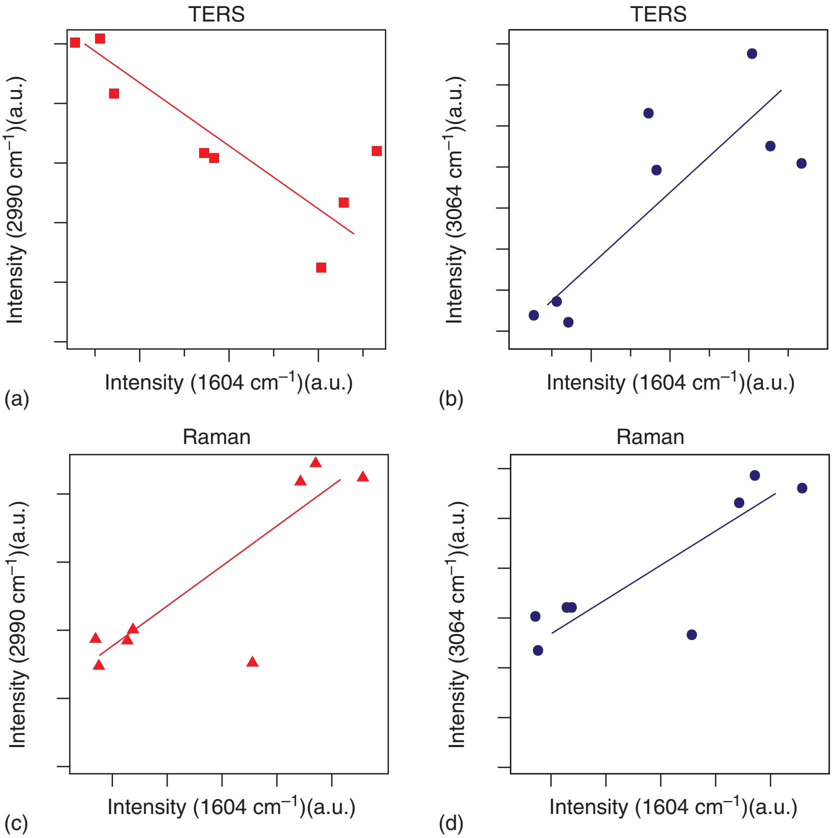

Figure 1.35 Peak intensity plots of (a) the vinyl band (2990 cm^{-1}) vs. the G band (1604 cm^{-1}) in the TERS spectrum, (b) the phenyl band (3064 cm^{-1}) vs. the G band (1604 cm^{-1}) in the TERS spectrum, (c) the vinyl band (2990 cm^{-1}) vs. the G band (1604 cm^{-1}) in the normal Raman spectrum, and (d) the phenyl band (3064 cm^{-1}) vs. the G band (1604 cm^{-1}) in the normal Raman spectrum. Source: Suzuki et al. [76].

(Figure 1.33a), both signals at 2990 (vinyl) and 3064 (phenyl) cm^{-1} increase with increase in the intensity of the 1604 cm^{-1} signal (Figure 1.35c,d). These results suggest that the local distribution of polymer nanocomposites at the interface between the polymer and the filler is different from that of polymer areas without CNTs. The depth resolution of TERS is much smaller than its spatial resolution (approximately 100 nm). It is known that the intensity of the TERS signal decays exponentially from the surface, having a decay length of 2.8 nm. Hence, TERS experiments measure a region several nanometers in depth from the surface of the nanocomposites.

Figure 1.36 illustrates a schematic diagram of the expected surface structure of SBR/MWCNT nanocomposites as proposed by Suzuki et al. [76], specifically, (a) far from the MWCNT area and (b) near the CNT area. In the polymer areas where MWCNTs are not located (a), it is very likely that the C = C groups and phenyl rings

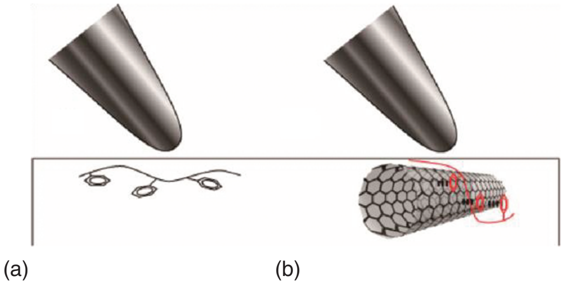

Figure 1.36 Schematic diagram of the surface structure of SBR/MWCNT nanocomposites: (a) far from and (b) near the CNT area. At the interface between the polymer and the filler, the phenyl ring should be oriented perpendicular to the surface through π–π interactions between the CNT and the phenyl ring. Source: Suzuki et al. [76].

are parallel to the polymer surface. In this orientation, the C = C signal is much more enhanced than that of the phenyl ring. On the other hand, at the interface of the polymer and the filler (Figure 1.36b), it is very likely that MWCNTs interact with the phenyl rings of the polymer through π–π interactions. These interactions induce differences in the orientation of the polymer chains and their side residues. The orientation of the phenyl rings at the interface may be nearly perpendicular to the surface because of the π–π interactions between the CNTs and the phenyl rings shown in Figure 1.36b.

1.4 Perspectives for Polymer Spectroscopy

In this chapter, we have reported a brief history of polymer spectroscopy, its roles and present status, and some examples of applications of polymer spectroscopy. In the last section, we discuss the perspectives for polymer spectroscopy.

Surface IR spectroscopy should be developed further for studies on polymer surfaces, interfaces, and thin films [20]. Even today, surface IR spectroscopy is used extensively for the study of polymer surface structure, interaction with substrates, and molecular orientation. ATR, external reflection, and RA spectroscopy are representative of the surface IR spectroscopy of polymers. Spectral analysis methods for surface IR spectroscopy have also been developed. For example, Hasegawa [78] proposed the multi-angle incidence resolution spectrum (MEIRS), which has recently been used extensively for the analysis of surface IR spectra. Surface IR spectroscopy will be further developed in combination with imaging techniques and X-ray techniques such as grazing incident X-ray diffraction (GIXD).

FUV spectroscopy was first applied to polymer studies several years ago (Section 1.2 and Chapter 6). Because FUV spectroscopy is an electronic spectroscopy technique, it provides different information about polymer structure and functions from vibrational spectroscopy. Notably, polymers usually do not absorb in the DUV and UV regions and absorb only in the FUV region. Therefore, FUV spectroscopy is unique for investigating the electronic structure and electronic transitions of polymers. Moreover, it is useful, for example, for studies of polymer nanocomposites, polymers absorb in the FUV region, whereas nanomaterials such as graphene and carbon nanotubes absorb mostly in the DUV and UV regions; thus, one can investigate the electronic structure of a polymer and a carbon nanomaterial independently. Thus, FUV spectroscopy is very promising for the electronic spectroscopy of polymers (Chapter 6).

Currently, imaging techniques are very popular in various fields (Chapters 2 and 5). In polymer science, imaging techniques are used in combination with IR, Raman, NIR, and terahertz spectroscopy. Each imaging spectroscopy technique has different characteristics and advantages for polymer research. However, almost all imaging studies involve 2D imaging. Although we have introduced one example of the 3D imaging of polymers in this chapter, 3D imaging studies are rather rare. As a next-generation technique for polymer spectroscopy, 3D imaging is very important.

Nanospectroscopy, such as TERS and AFM-IR (nano-IR), is also a developing technique. AFM-IR consists of an IR spectrometer and SPM [79]. Originally, the term AFM-IR was used to describe a method that combines a tunable free-electron laser with an AFM equipped with a sharp probe that enables the measurement of the IR absorption of a sample in a nanoscale area. The spatial resolution of AFM-IR reaches 10 nm, which is almost as high as that of TERS. AFM-IR has recently been used for studies of polymers, polymer blends, and polymer nanocomposites, particularly multilayer films and thin films.

Theoretical calculations of electronic and vibrational spectra are particularly important for the development of polymer spectroscopy, and computational molecular spectroscopy is being developed. Of recent note is the development of anharmonic calculations. Because of this, one can reproduce Raman and IR spectra more precisely, and, moreover, one can reproduce NIR spectra that consist of bands arising from overtones and combinations. Moreover, computer power is getting more powerful while computational resources (particularly time and cost) are becoming increasingly smaller, and thus, it is expected that quantum chemical calculations of polymer spectra will become more popular.

Further, it is likely that NIR spectroscopy for polymer studies will advance in two directions. One is industrial applications, and NIR spectroscopy has already been used in many applications in the polymer industry (Chapter 5); for example, the online analysis of polymers, polymer coating, process monitoring, and process control of synthetic textiles. Online analysis and process control will develop further with the introduction of new software technologies, such as artificial intelligence (AI) and machine learning. NIR spectroscopy should also be developed for polymer structural analysis. In this regard, the development of anharmonic calculations will play an important role, which will make the analysis of overtones and combinations easier; thus, more concrete information about the band assignments in the NIR region will be obtained, enabling deeper studies of polymer structures, interactions, and reactions.

References

1 Nyquist, R.A. (1961). *Infrared Spectra of Plastics and Resins*, 2e. Dow Chemical Co.

2 Zbinden, R. (1964). *Infrared Spectroscopy of High Polymers*. Academic Press.

3 Henniker, C.J. (1967). *Infrared Spectrometry of Industrial Polymers*. Academic Press.

4 Siesler, H.W. and Holland-Moritz, K. (1980). *Infrared and Raman Spectroscopy of Polymers*. Dekker.

5 Tadokoro, H. (1990). *Structure of Crystalline Polymers*. Krieger Pub. Co.

6 Coleman, M.M., Graf, J.F., and Painter, P.C. (1991). *Specific Interactions and the Miscibility of Polymer Blends*. Technical Publishing Co.

7 Koenig, J.L. (1999). *Spectroscopy of Polymers*, 2e. Elsevier.

8 Brame, E.G. (2012). *Applications of Polymer Spectroscopy*. Academic Press.

9 Thomas, S. and Rouxel, D. (2016). *Spectroscopy of Polymer Nanocomposites*. Elsevier.

10 Ozaki, Y. and Kawata, S. (eds.) (2015). *Far- and Deep-Ultraviolet Spectroscopy*. Springer.

11 Morisawa, Y., Tanabe, I., and Ozaki, Y. (2018). Advances in far-ultraviolet spectroscopy in the solid and liquid states. In: *Frontiers and Advances in Molecular Spectroscopy* (ed. J. Laane), 251–285. Elsevier.

12 Ozaki, Y., Morisawa, Y., Tanabe, I., and Beć, K.B. (2021). *Spectrochim. Acta A* 253: 119549.

13 (a) Morisawa, Y., Yasunaga, M., Sato, H. et al. (2014). *J. Phys. Chem. B* 118: 11855. (b) Beć, K.B., Morisawa, Y., Kobashi, K. et al. (2018). *Phys. Chem. Chem. Phys.* 20: 8859.

14 Ueno, N., Wakabayashi, T., Sato, H., and Morisawa, Y. (2019). *J. Phys. Chem. A* 123: 10746.

15 Ozaki, Y., Huck, C.W., Tsuchikawa, S., and Elgensen, S.B. (eds.) (2020). *Near-Infrared Spectroscopy*. Springer.

16 Ozaki, Y., McClure, W.F., and Christy, A.A. (eds.) (2007). *Near-Infrared Spectroscopy in Food Science and Technology*. Wiley.

17 Ozaki, Y. (2012). *Anal. Sci.* 28: 545.

18 Griffiths, P.R. and de Haseth, J.A. (1986), 2e. (2007)). *Fourier Transform Infrared Spectroscopy*, 1e. Wiley Interscience.

19 (a) Christy, A.A., Ozaki, Y., and Gregoriou, V.G. (2001). *Modern Fourier-Transform Infrared Spectroscopy*. Elsevier. (b) Gunzler, H. and Gremlich, H.-U. (2002). *IR Spectroscopy*. Wiley-VCH.

20 Hasegawa, T. (2017). *Quantitative Infrared Spectroscopy for Understanding of a Condensed Matter*. Springer.

21 Finch, A., Gates, P.N., Radcliffe, K. et al. (1970). *Chemical Applications of Far-Infrared Spectroscopy*. Academic Press.

22 Moller, K.D. and Rothschild, W.G. (1971). *Far-Infrared Spectroscopy*. Wiley Interscience.

23 Peiponen, K.-E., Zeitler, J.A., and Kuwata-Gonokami, M. (eds.) (2013). *Terahertz Spectroscopy and Imaging*. Springer.

24 Coutaz, J.-L., Garet, F., and Wallace, V. (2018). *Principles of Terahertz Time-Domain Spectroscopy*. Pan Stanford.

25 Baxter, J.B. and Guglietta, G.W. (2011). *Anal. Chem.* 83: 4342.

26 Ozaki, Y. (2019). *Bull. Chem. Soc. Jpn.* 92: 629.

27 Grasselli, J.G. and Bulkin, B.J. (1991). *Analytical Raman Spectroscopy*. Wiley-Interscience.

28 Long, D.A. (2002). *The Raman Effect*. Wiley.

29 McCreery, R.L. (2000). *Raman Spectroscopy for Chemical Analysis*. Wiley Interscience.

30 Smith, E. and Dent, G. (2019). *Modern Raman Spectroscopy*. Wiley.

31 Schlücker, S. (ed.) (2010). *Surface-Enhanced Raman Spectroscopy: Analytical, Biophysical and Life Science Applications*. Wiley-VCH.

32 Ozaki, Y., Kneipp, K., and Aroca, R. (eds.) (2014). *Frontiers of Surface-Enhanced Raman Scattering*. Wiley.

33 Kneipp, K., Ozaki, Y., and Tian, Z.-Q. (eds.) (2018). *Recent Developments in Plasmon-Supported Raman Spectroscopy*. World Scientific.

34 Zoubir, A. (ed.) (2012). *Raman Imaging, Techniques and Applications*. Springer.

35 Kirkwood, J.G. (1939). *J. Chem. Phys.* 7: 506.

36 Whitcomb, S.E., Nielsen, H.H., and Thomas, L.H. (1940). *J. Chem. Phys.* 8: 143.

37 (a) Shimanouchi, T. and Mizushima, S. (1949). *J. Chem. Phys.* 17: 1102.
(b) Shimanouchi, T. (1949). *J. Chem. Phys.* 17: 245, 734, and 848.

38 Shimanouchi, T. (1955). *J. Chem. Phys.* 23: 2465. and 25, 660 (1956).

39 (a) Krimm, S. (1954). *J. Chem. Phys.* 22: 567. (b) Krimm, S., Liang, C.Y., and Sutherland, G.B.B.M. (1956). *J. Chem. Phys.* 25: 549.

40 Eliot, A. (1959). The infrared spectra of polymers. In: *Advances in Spectroscopy*, 1e (ed. H.W. Thomson), 214–287. Interscience.

41 Hummel, D.O. (1966). *Infrared Spectra of Polymers in the Medium and Long Wave Regions*. Wiley Interscience.

42 Schachtschneider, J.H. and Snyder, R.G. (1963). *Spectrochim. Acta* 19: 117.

43 Tasumi, M. and Shimanouchi, T. (1965). *J. Chem. Phys.* 43: 1245.

44 (a) Sugeta, H., Miyazawa, T., and Kajiura, T. (1969). *J. Polym. Sci. B Polym. Lett.* 7: 251. (b) Matsuura, H. and Miyazawa, T. (1969). *J. Polym. Sci. A* 2: 1735.

45 Kitagawa, T. and Miyazawa, T. (1972). *Adv. Ploym. Sci.* 9: 336.

46 Kakida, H., Makino, D., Chatani, Y. et al. (1970). *Macromolecules* 3: 569.

47 Tadokoro, H., Takahashi, Y., Chatani, Y., and Kakida, H. (1967). *Makromol. Chem.* 106: 96.

48 Krimm, S. and Bank, M.I. (1965). *J. Chem. Phys.* 42: 4059.

49 Mizushima, S. and Shimanouchi, T. (1949). *J. Am. Chem. Soc.* 71: 1320.

50 Hendra, P.J. (1969). *Adv. Polym. Sci.* 6: 151.

51 (a) Koenig, J.L. and Druesdow, D.J. (1969). *J. Polym. Sci.* A2: 1075. (b) Koenig, J.L. and Angood, A.C. (1970). *J. Polym. Sci.* A8: 1787.

52 Schaufele, R.F. and Shimanouchi, T. (1967). *J. Chem. Phys.* 47: 3605.

53 Stroble, G.R. and Eckel, R. (1976). *J. Polym Sci. Polym Phys. Ed.* 14: 913.

54 Hsu, S.L. and Krimm, S. (1976). *J. Appl. Phys.* 47: 4265. and 48, 4013 (1977).

55 Miller, R.G.J. and Willis, H.A. (1956). *J. Appl. Chem.* 6: 385.

56 (a) Takeuchi, T., Tsuge, S., and Sugimura, Y. (1968). *J. Polym. Sci. A* 1: 3415. (b) Tosi, C. (1968). *Makromol. Chem.* 112: 303.

57 (a) Hoshina, H., Morisawa, Y., Sato, H. et al. (2010). *Appl. Phys. Lett.*: 96. http://www.ncbi.nlm.nih.gov/pubmed/011907. (b) Yamamoto, S., Morisawa, Y., Sato, H. et al. (2013). *J. Phys. Chem. B* 117: 2180. (c) Yamamoto, S., Miyada, M., Sato, H. et al. (2017). *J. Phys. Chem. B* 121: 1128. (d) Yamamoto, S., Onishi, E., Sato, H. et al. (2019). *J. Phys. Chem. B* 123: 536. (e) Funaki, C., Toyouchi, T., Hoshina, H. et al. (2017). *Appl. Spectrosc.* 71: 1537.

58 Bakeev, K.A. (2010). *Process Analytical Technology*, 2e. Wiley.

59 Kessler, R.W. and Kessler, W. (2020). Inline and online process analytical technology with an outlook for the petrochemical industry. In: *Near-Infrared Spectroscopy* (eds. Y. Ozaki, C.W. Huck, S. Tsuchikawa and S.B. Engelsen), 553. Springer.

60 Czarnecki, M.A., Beć, K.B., Grabska, J. et al. (2020). Overview of application of NIR spectroscopy to physical chemistry. In: *Near-Infrared Spectroscopy* (eds. Y. Ozaki, C.W. Huck, S. Tsuchikawa and S.B. Engelsen), 297. Springer.

61 (a) Beć, K.B., Grabska, J., and Hofer, T.S. (2020). Introduction to quantum vibrational spectroscopy. In: *Near-Infrared Spectroscopy* (eds. Y. Ozaki, C.W. Huck, S. Tsuchikawa and S.B. Engelsen), 83. Springer. (b) Beć, K.B., Grabska, J., Huck, C.W., and Ozaki, Y. (2019). Quantum mechanical simulation of near-infrared spectra: application in physical chemistry and analytical chemistry. In: *Molecular Spectroscopy: A Quantum Chemistry Approach* (eds. Y. Ozaki, M.J. Wojcik and J. Popp), 327. Wiley.

62 Dong, J., Nakashima, K., and Ozaki, Y. (1997). *Macromolecules* 30: 1111.

63 Walczak, W.J., Hoagland, D.A., and Hsu, S.L. (1992). *Macromolecules* 25: 7317.

64 Bardet, L., Cassanas-Fabre, G., and Alain, M. (1975). *J. Mol. Struct.* 24: 153.

65 Ng, J.B. and Shurvell, H.F. (1987). *J. Phys. Chem.* 91: 496.

66 Tanaka, N., Kitano, H., and Ise, N. (1990). *J. Phys. Chem.* 94: 6290.

67 Coleman, M.M., Graf, J.F., and Painter, P.C. (1991). *Specific Interactions and the Miscibility of Polymer Blends*, 328. Technomic Publishing Inc.

68 Song, Y.P., Yarwood, J., Tsibouklis, J. et al. (1992). *Langmuir* 8: 262.

69 Sun, L., Kepley, L.J., and Crooks, R.M. (1992). *Langmuir* 8: 2101.

70 Tadokoro, H., Kobayashi, M., Yoshidome, H. et al. (1968). *J. Chem. Phys.* 49: 3359.

71 Malta, V., Cojazzi, G., Fichera, A. et al. (1979). *Eur. Polym. J.* 15: 765.

72 Frank, W.F.X. and Fiedler, H. (1979). *Infrared Phys.* 19: 481.

73 Shimoyama, M., Ninomiya, T., Sano, K. et al. (1998). *J. NIR Spectrosc.* 6: 317.

74 Hu, J., Wang, J., Wang, M. et al. (2019). *Polymer* 172: 1.

75 Vantasin, S., Ji, W., Tanaka, Y. et al. (2016). *Angew. Chem. Int. Ed.* 55: 8391.

76 Suzuki, T., Yan, X., Kitahama, Y. et al. (2013). *J. Phys. Chem. C* 117: 1436.

77 (a) Bokobza, L. (2011). *Macromol. Symp.* 305: 1. (b) Bokobza, L. (2007). *Polymer* 8: 4907.

78 Hasegawa, H. (2007). *J. Phys. Chem. B* 106: 4385. (2002) Anal. Chem. 79, 4112.

79 (a) Hammiche, A., Pollock, H.M., Reading, M. et al. (1999). *Appl. Spectrosc.* 53: 810. (b) Anderson, M.S. (2000). *Appl. Spectrosc.* 54: 349.